15ATC-0250

Development of Variable Camber Continuous Trailing Edge Flap for Performance Adaptive Aeroelastic Wing

Nhan Nguyen, Upender Kaul
NASA Ames Research Center
Moffett Field, CA 94035
Sonia Lebofsky, Eric Ting, Daniel Chaparro
Stinger Ghaffarian Technologies, Inc.
NASA Ames Research Center
Moffett Field, CA 94035
James Urnes
Boeing Research and Technology
St. Louis, MO 63134

Abstract

This paper summarizes the recent development of an adaptive aeroelastic wing shaping control technology called variable camber continuous trailing edge flap (VCCTEF). As wing flexibility increases, aeroelastic interactions with aerodynamic forces and moments become an increasingly important consideration in aircraft design and aerodynamic performance. Furthermore, aeroelastic interactions with flight dynamics can result in issues with vehicle stability and control. The initial VCCTEF concept was developed in 2010 by NASA under a NASA Innovation Fund study entitled "Elastically Shaped Future Air Vehicle Concept," which showed that highly flexible wing aerodynamic surfaces can be elastically shaped in-flight by active control of wing twist and bending deflection in order to optimize the spanwise lift distribution for drag reduction. A collaboration between NASA and Boeing Research & Technology was subsequently funded by NASA from 2012 to 2014 to further develop the VCCTEF concept.

This paper summarizes some of the key research areas conducted by NASA during the collaboration with Boeing Research and Technology. These research areas include VCCTEF design concepts, aerodynamic analysis of VCCTEF camber shapes, aerodynamic optimization of lift distribution for drag minimization, wind tunnel test results for cruise and high-lift configurations, flutter analysis and suppression control of flexible wing aircraft, and multi-objective flight control for adaptive aeroelastic wing shaping control.

1 INTRODUCTION

Air vehicles are typically designed to maintain sufficient structural rigidity for safe load-carrying capacity. Modern engineered materials such as composites have begun to appear in new airframe design that can provide less structural rigidity while maintaining the same load-carrying capacity. An example of light-weight airframe design is the Boeing 787 Dreamliner aircraft, which has highly flexible wing structures in comparison to those in older-generation aircraft. As wing flexibility increases, aeroelastic interactions with aerodynamic forces and moments become an increasingly important consideration in aircraft design and aerodynamic performance. Furthermore, aeroelastic interactions with flight dynamics can result in issues with vehicle stability and control. Modern aircraft such as the Boeing 787 have technologies to compensate for adverse aeroelastic interactions with flight performance and dynamics. Airbus also begins to deploy similar technologies called aerodynamic re-optimization on recent aircraft production.

To address the performance aspects of wing flexibility in transport design, NASA developed an innovative wing shaping control concept called the variable camber continuous trailing edge flap (VCCTEF) in 2010 in a NASA Innovation Fund study sponsored by NASA Innovative Partnerships Program Office [1, 2, 3]. This study, entitled "Elastically Shaped Future Air Vehicle Concept," showed that highly flexible wing aerodynamic surfaces can be elastically shaped in-flight by active control of wing twist and bending deflection in order to optimize the local angle of attack of wing sections to improve aerodynamic efficiency through

drag reduction during cruise and enhanced lift performance during take-off and landing.

Subsequently, this study has been further investigated under three NASA projects since 2011: the Subsonic Fixed Wing (SFW) project in 2011, the Fixed Wing (FW) project from 2012 to 2014, and currently the Advanced Air Transport Technology (AATT) project since 2015. Boeing Research and Technology which collaborated with NASA in the 2010 study was funded by NASA Fixed Wing Project to continue collaboration with NASA under a two-phase study to further develop the VCCTEF concept. The Phase I study was performed during 2012 to revise the initial VCCTEF concept and develop actuation mechanisms [4]. The Phase II study was a two-year effort from 2013 to 2014. The objectives of the Phase II study were to conduct aeroelastic analysis and flutter suppression control as well as two wind tunnel tests of a cruise configuration in 2013 and a high-lift configuration in 2014 in a low-speed wind tunnel at the University of Washington Aeronautical Laboratory (UWAL) [5].

This paper summarizes some of the key research areas conducted by NASA in collaboration with Boeing Research and Technology and UWAL. These areas include VCCTEF design concepts, aerodynamic analysis of VCCTEF camber shapes using RANS OVERFLOW CFD tool, aerodynamic optimization of lift distribution for drag minimization using a coupled FEM vortex-lattice aerodynamic framework with nonlinear transonic correction, flutter analysis and flutter suppression control of flexible wing aircraft, and multi-objective flight control for the VCCTEF.

2 VCCTEF CONCEPT

Aeroelastic deflection can affect aircraft aerodynamics. As an aircraft cruises, fuel is burned and the wing loading is reduced, thereby causing the wing shape to change. The change in wing shape can cause a drag penalty since the wing shape no longer retains its optimal design shape. This particularly can be an important issue for lightweight flexible airframes. Thus, aircraft with flexible wing structures can potentially become less fuel-efficient if there is no mechanism to compensate for aeroelastic deflection.

The objective of wing shaping control is to restore the wing shape back to an optimal shape through flap and or slat deployments. However, the drag penalty due to flap and slat deflections can negate any benefit attained from wing shaping control. The initial study in 2010 explored the use of distributed conventional flap and slat systems for wing shaping control. In a conventional flap design, individual flaps are actuated independently. As a result, the trailing edge of a wing formed by the flap deflections is discontinuous. This discontinuity is a source of drag penalty as well as acoustic emissions. Aerodynamic calculations show that the drag penalty due to the conventional flap system could be substantial [1]. One way to reduce the drag penalty is to use a single flap surface over a wide wing span. However, this would compromise the flexibility and effectiveness of wing shaping control. Thus, a new low-drag wing shaping control device was proposed in the initial study. This flap system is referred to as a variable camber continuous trailing edge flap (VCCTEF) system, as shown in Figures 1 to 3, which appears to provide a significant drag reduction over a conventional flap system based on the initial study in 2010 [1].

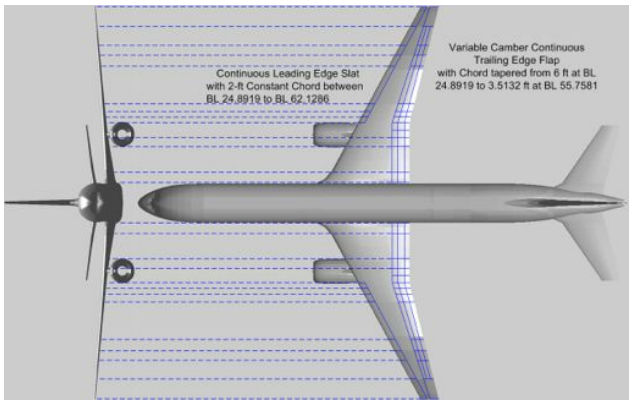

Figure 1: Planform of Variable Camber Continuous Trailing Edge Flap Concept

The two main features of this flap concept are:

1. Variable camber - The flap chord is comprised of three chordwise segments of equal chord length as shown in Figure 2. These three flap segments are actuated in unison when a flap deflection command is given. Each flap segment is deflected by an angle equal to one third of the commanded flap deflection relative to each other. For example, for a commanded flap deflection of $12°$, flap segment 1 which is positioned next to the wing is deflected $4°$, flap segment 2 that follows flap segment 1 is deflected $8°$, and flap segment 3 at the trailing edge is deflected by $12°$. This deflection achieves a circular arc trailing edge camber as follows:

$$f_1 = \frac{f_c}{3} \tag{1}$$

$$f_2 = \frac{2f_c}{3} \tag{2}$$

$$f_3 = f_c \tag{3}$$

where f_c is the commanded flap deflection.

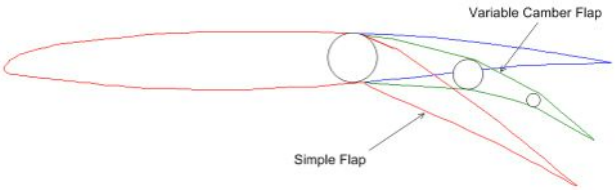

Figure 2: Three-Segment Variable Camber Flap

The camber angle of the flap is the difference between between f_3 and f_1. Thus, the variable camber angle $\chi = 2f_c/3$ is a function of the commanded flap deflection. A cambered flap is more effective in producing lift than a straight plain flap. That is, it should produce higher lift-to-drag ratios (L/D). Other types of camber could also be specified instead of a circular arc camber.

The variable camber flap generally produces about the same downwash as a simple plain flap deflected by the same angle, as seen in Figure 2. However, the normal surface area of the variable camber flap exposed to the flow field is significantly reduced. Thus, the drag reduction benefit of the variable camber flap is realized since the pressure drag across the flap surface is reduced due to less exposed normal surface area.

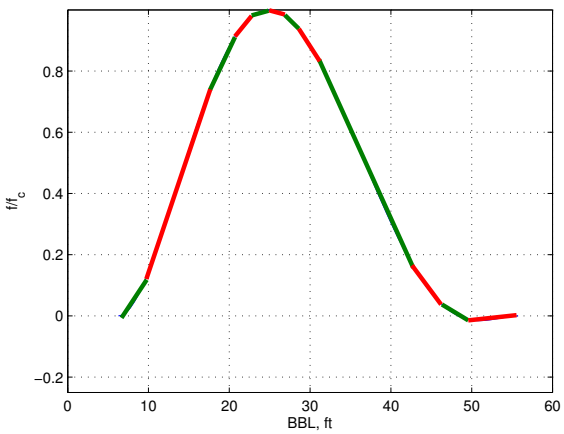

Figure 3: Continuous Trailing Edge Flap Sections

2. Continuous trailing edge - The continuous trailing edge is comprised of 12 spanwise sections to form a continuous trailing edge, as shown in Figure 3, when the flap is deflected. This continuous trailing edge would eliminate vortices which otherwise would have formed at the conventional flap discontinuity at the trailing edge. By reducing or eliminating vortex formation, viscous drag could be reduced and acoustic emissions from turbulence could be attenuated. The material and design methodology used to fabricate this flap system must be able to provide some degree of structural compliance due to differential flap deflections that each flap spanwise section would need to maintain a continuous trailing edge. This feature provides a further drag reduction benefit in addition to the variable camber chordwise flap segmentation concept.

Figure 4 illustrates the VCCTEF installed on a transport aircraft.

The VCCTEF is envisioned to be a multi-functional flight control surface capable of

- Aerodynamic re-optimization of the flexible wing to obtain changes in lift-to-drag ratios for cruise drag reduction throughout the flight envelope
- High-lift performance for take-off and landing
- Aeroservoelastic control of aeroelastic wing modes
- Load alleviation control for gust and maneuver loads
- Rigid-body flight control for pitch and roll

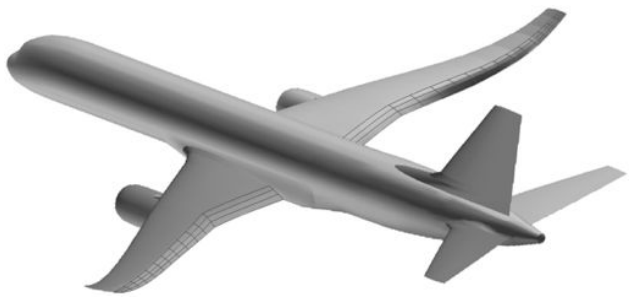

Figure 4: Transport Aircraft with Variable Camber Continuous Trailing Edge Flap

The Phase I study entitled “Development of Variable Camber Continuous Trailing Edge Flap System” [4] was conducted by Boeing Research and Technology in 2011 under the SFW Project. This study built upon the development of the VCCTEF system for NASA Generic Transport Model (GTM) which is essentially based on the B757 airframe, employing light-weight shaped memory alloy (SMA) technology for actuation and three individual chordwise segments shaped to provide a variable camber to the flap, as defined in the initial study in 2010. The spanwise flap is divided into 14 sections attached to the outer wing and 3 sections

attached to the inner wing. Each 24-inch section has three cambered flap segments that can be individually commanded. These cambered flaps are joined to the next section by a flexible transition material installed with the same shape as the camber and thus providing continuous flaps throughout the wing span with no drag producing gaps [6]. This continuous trailing edge flap design combined with the flap camber result in lower drag increase during flap deflections. In addition, it also offers a potential noise reduction benefit. This results in the ability to control the wing twist shape as a function of span, resulting in a change to the wing twist to establish the best lift-to-drag ratio (L/D) at any aircraft gross weight or mission segment. Current wing twist on commercial transports is permanently set for one cruise configuration, usually for a 50% loading or mid-point on the gross weight schedule. The VCCTEF offers different wing twist settings for each gross weight condition and also different settings for climb, cruise and descent, a major factor in obtaining best L/D conditions.

The VCCTEF concept developed by Boeing Research and Technology in conjunction with NASA is illustrated in Figure 5.

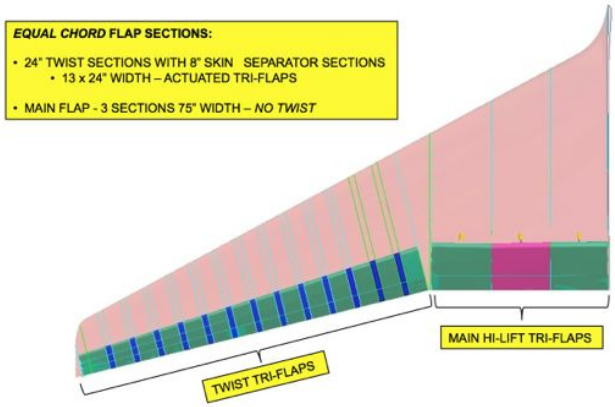

Figure 5: Wing Configured with the Variable Camber Continuous Trailing Edge Flap

A major goal is to develop a light-weight flap control system that has a significant weight advantage as compared to current flap screw-jack actuators. Hydraulic, electric and Shape Memory Alloy (SMA) torque rod actuation were evaluated with the result that the SMA actuation has the best weight advantage, as shown in Figure 6. Moreover, the use of hinge line actuation eliminates the large and heavy external mounted actuators, and permits all actuators to be interior to the wing and flap mold lines, thus contributing to the overall drag reduction goal. SMA actuators can deliver large hinge moments, but generally move at a slow rate. The outer wing flap uses the full-span third camber segment as a roll command effector and as a control device for suppressing aeroelastic wing structural dynamic modes, both requiring high rates which can be met by electric actuators [7]. This is shown in Figure 7.

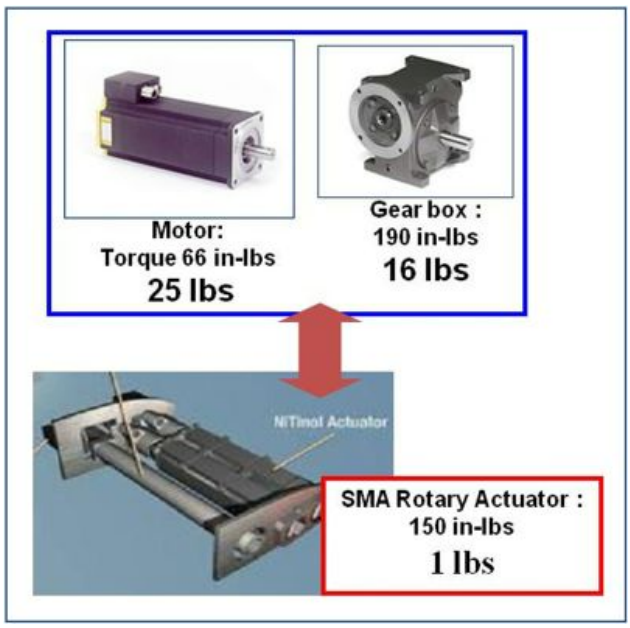

Figure 6: Weight Comparison between Shape Memory Alloy Actuators and Electric Motor Actuators

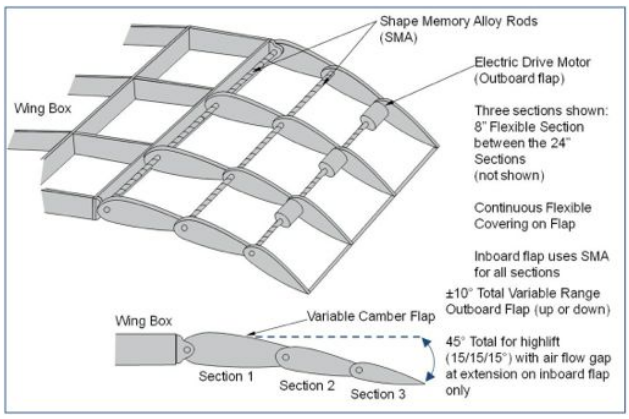

Figure 7: Shape Memory Alloy Torque Rod and Electric Drive Actuation for VCCTEF Control

The Phase II study entitled "Development of Variable Camber Continuous Trailing Edge Flap System for B757 with a More Flexible Wing" which was conducted in 2012 under the FW Project to investigate the effectiveness of the VCCTEF for transport aircraft with increased wing flexibility [5]. In particular, the baseline wing stiffness of the GTM is arbitrarily reduced by 50% thereby doubling the wing flexibility. Aerodynamic optimization, flutter analysis, and flutter

suppression control were studied to assess the effect of the increased wing flexibility [8]. Another objective of the Phase II study is to conduct a trade study with an alternative VCCTEF design which employs fewer flap elements for weight savings. Figure 8 illustrate the alternative VCCTEF concept which reduces the number of cambered flap segments from three to two and the number of spanwise section from 14 to 8 for the outer wing. Each spanwise section is 50 inches in length and are separated by 5-inch elastomer transition material. As part of the Phase II study, two wind tunnel tests were conducted in the UWAL to perform initial assessments of the VCCTEF for cruise drag reduction as well as high-lift performance. The cruise configuration test was conducted in 2013 [9, 10] and the high-lift configuration test was conducted in 2014 [11, 12].

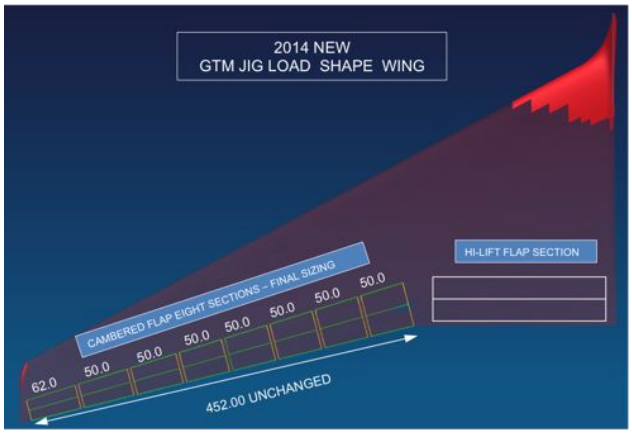

Figure 8: Alternative VCCTEF Concept with Fewer Flaps

3 2D CFD SIMULATIONS

As part of the trade study, a 2D airfoil CFD simulation is performed using RANS CFD code OVERFLOW [13]. The computational study examines flow over a 2D airfoil with various camber shapes and number of camber segments. In particular, the following airfoil configurations are studied:

Table 1: Definition of VCCTEF Configurations

VCCTEF Configuration	Notation	Flap 1	Flap 2	Flap 3
Three-Segment Parabolic Arc Camber	VCCTEF123	$1°$	$2°$	$3°$
Three-Segment Circular Arc Camber	VCCTEF222	$2°$	$2°$	$2°$
Three-Segment Semi-Rigid Camber	VCCTEF321	$3°$	$2°$	$1°$
Two-Segment Circular Camber	VCCTEF22	$2°$	$2°$	
Plain Flap	VCCTEF6	$6°$		

The deflection of a flap segment is specified as a relative deflection in relation to the previous flap segment. Thus, the configuration VCCTEF123 denotes a configuration whereby the deflection of flap segment 1 is $1°$ relative to the fixed wing section, the deflection of flap segment 2 is $2°$ relative to flap segment 1 or $3°$ relative to the fixed wing section, and the deflection of flap segment 3 is $3°$ relative to flap segment 2 or $6°$ relative to the fixed wing section. Thus all the configurations have the same flap deflection of $6°$ at the trailing edge flap segment relative to the fixed wing section.

The 2D wing section is selected to be at the wing break station on the GTM wing and is normal to the wing leading edge to account for the wing sweep, as shown in Figure 9. The flow conditions are $M_\infty = 0.7$ which accounts for the leading edge sweep angle, $Re = 9 \times 10^6$, and $\alpha = 0° - 5°$.

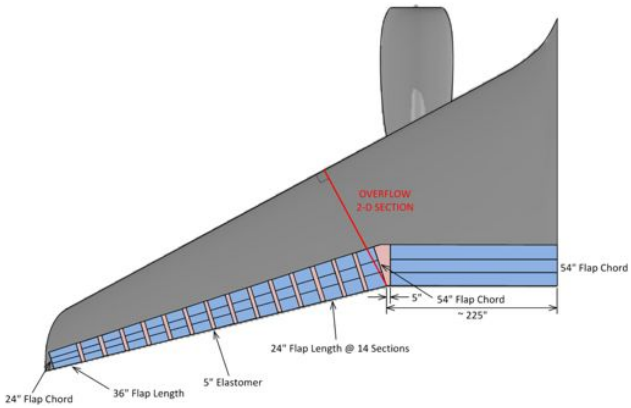

Figure 9: 2-D Section with VCCTEF for OVERFLOW Simulations

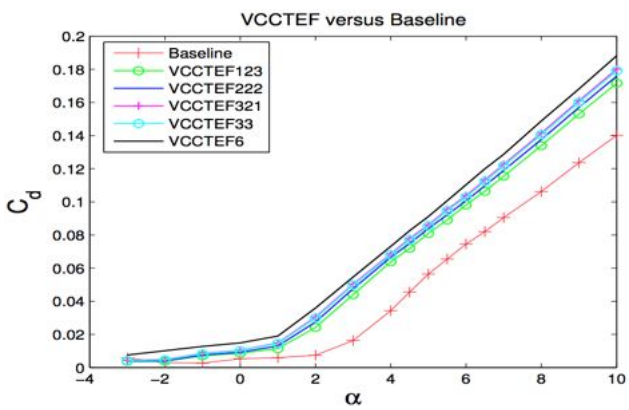

Figure 10: Drag Coefficient vs. Angle of Attack Computed by OVERFLOW

Figure 10 shows the drag coefficient as a function of the angle of attack. At a given angle of attack, the plain flap configuration VCCTEF6 has the highest drag and the parabolic-arc-camber or VCCTEF123 configuration has the lowest drag. This is consistent

with the profile drag of the plain flap configuration VCCTEF6 being the largest based on the flap projected area normal to the flow direction. Figure 11 shows the lift coefficient as a function of the angle of attack. The plain flap configuration VCCTEF6 produces the largest incremental lift while the converse is true with the parabolic-arc-camber configuration VCCTEF123. The lift-to-drag ratios of the VCCTEF configurations are plotted in Figure 12.

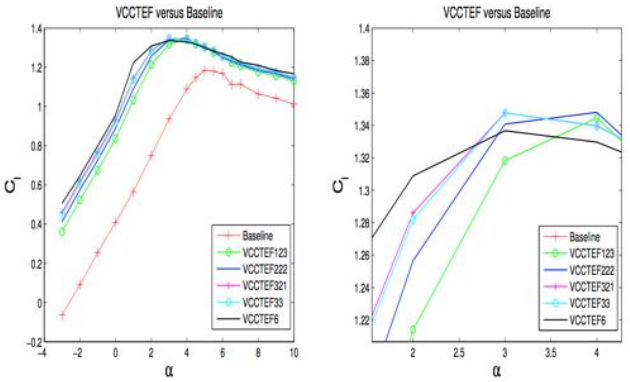

Figure 11: Lift Coefficient vs. Angle of Attack Computed by OVERFLOW

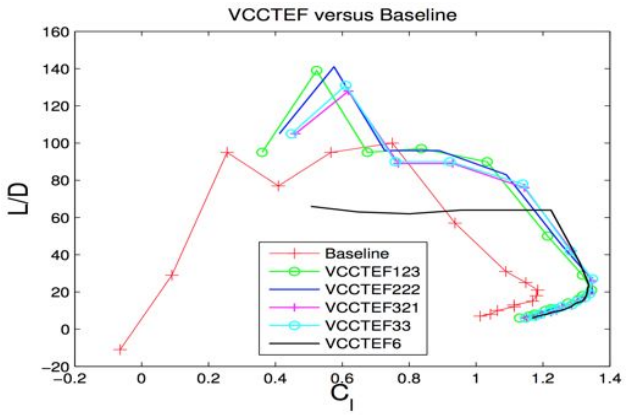

Figure 12: Lift-to-Drag Ratio Computed by OVERFLOW

The plain flap configuration VCCTEF6 has the lowest lift-to-drag ratio which is also less than the baseline clean airfoil configuration. Both the circular-arc-camber configuration VCCTEF222 and the parabolic-arc-camber configuration VCCTEF123 have the highest lift-to-drag ratios. This indicates that the circular-arc-camber VCCTEF is much more aerodynamically efficient than the plain flap in producing lift. The effect of number of cambered segments is also revealed in Figure 12. The two-segment circular-arc-camber configuration VCCTEF33 has lower lift-to-drag ratio than the corresponding three-segment circular-arc-camber configuration VCCTEF222, but has higher lift-to-drag ratio than the plain flap configuration VCCTEF6.

Assuming that the flow over the VCCTEF surfaces is entirely subsonic, then the downwash created by the VCCTEF deflection is expressed as

$$\Delta w_i = V_\infty \delta_i \tag{4}$$

where Δw_i is the incremental downwash and δ_i is the absolute deflection of the i-th flap segment of the VCCTEF.

The slope of the camber line is related to the downwash as

$$\frac{dz_i}{dx} = -\frac{\Delta w_i}{V_\infty} = -\delta_i \tag{5}$$

Based on thin-wing aerodynamic theory, the incremental lift coefficient produced by the VCCTEF is evaluated by the integral transform with a potential kernel function $f(\theta) = \cos\theta - 1$ as

$$\begin{aligned}\Delta C_l &= \frac{C_{l_\alpha}}{\pi}\int_{\theta_1}^{\pi} \frac{dz}{dx} f(\theta)\, d\theta \\ &= -\frac{C_{l_\alpha}}{\pi}\sum_{i=1}^{n}\int_{\theta_i}^{\theta_{i+1}} \delta_i (\cos\theta - 1)\, d\theta\end{aligned} \tag{6}$$

where θ_i is the transformed coordinate of the hinge position of the inner flap segment and

$$x = \frac{c}{2}(1 - \cos\theta) \tag{7}$$

This integral is evaluated as

$$\Delta C_l = \sum_{i=1}^{n} C_{l_\alpha} \frac{\partial\alpha}{\partial\delta_i}\delta_i \tag{8}$$

where C_{l_α} is the sectional lift curve slope and $\partial\alpha/\partial\delta_i$ is the angle of attack sensitivity or camber control derivative due to the VCCTEF flap deflection which is given by

$$\frac{\partial\alpha}{\partial\delta_i} = \left.\frac{\cos^{-1} c^* - \sqrt{1 - c^{*2}}}{\pi}\right|_{c_i^*}^{c_{i+1}^*} \tag{9}$$

with $c_i^* = 1 - 2x_i/c$, c is the airfoil chord, $x_i = c - (n + 1 - i)\, c_f$ is the flap hinge position of the i-th flap segment, and c_f is the flap chord of a cambered segment.

Table 2 is the comparison between the incremental lift prediction by OVERFLOW and the theoretical incremental lift from Eq. (8)

Table 2: Computed vs. Theoretical Incremental Lift Prediction

Configuration	ΔC_l, Computed	ΔC_l, Theory	% Difference
VCCTEF123	0.4617	0.4469	-3.21
VCCTEF222	0.5031	0.5024	-0.14
VCCTEF321	0.5444	0.5495	0.94
VCCTEF33	0.5360	0.5427	1.25
VCCTEF6	0.6203	0.6021	-2.93

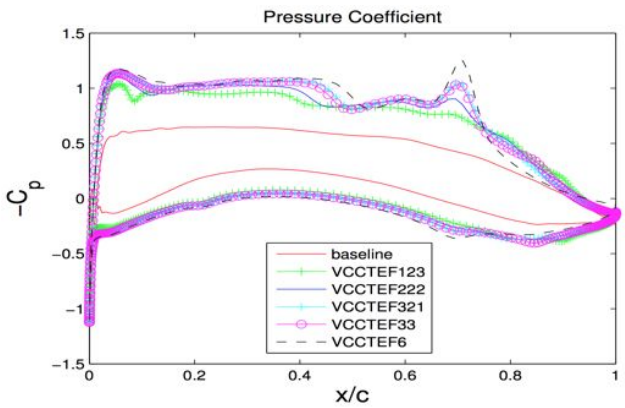

Figure 13: Pressure Coefficient Distribution on Airfoil Computed by OVERFLOW

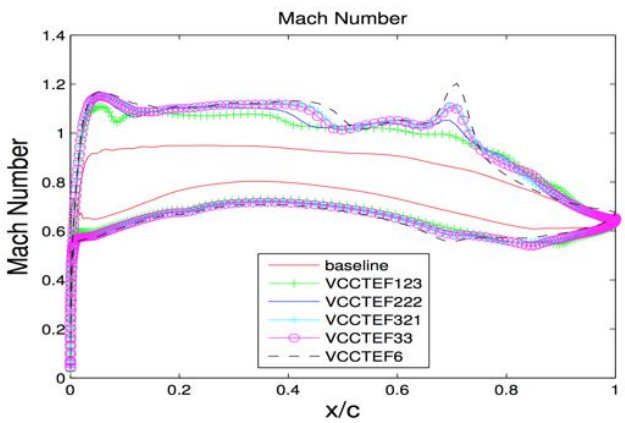

Figure 14: Mach Number Distribution on Airfoil Computed by OVERFLOW

Figures 13 and 14 are the plots of the pressure coefficients and Mach number distributions over the airfoil with the VCCTEF. It is noted that there is a shock formation at the first hinge line of the first cambered segment. The shock is strongest for the plain flap or VCCTEF6 configuration. The parabolic-arc-camber configuration VCCTEF123 has a gradual pressure recovery with a very slight shock structure near the leading edge. The circular-arc-camber configuration VCCTEF222 also has a favorable pressure recovery. There is a very weak shock structure at the first hinge line.

4 ADAPTIVE AEROELASTIC WING SHAPING CONTROL

Aeroelastic deflections of a flexible swept back wing can influence aircraft aerodynamic performance due to the wash-out twist effect resulting from wing bending and torsional twist. At off-design flight conditions, the wing lift distribution may deviate substantially from the ideal elliptical lift distribution due to the aeroelastic deflections. Adaptive aeroelastic wing shaping control is a performance adaptive aeroelastic wing technology that provides aeroelastic compensation to reduce the adverse effect of aeroelasticity on aerodynamic performance. The VCCTEF can be used to modify the spanwise lift distribution of a wing in order to restore the ideal elliptical lift distribution throughout a flight envelope.

The aeroelastic angle of attack of a wing section can be expressed as [10]

$$\alpha_c(y) = \alpha - \alpha_i(y) - \gamma(\bar{y})\cos\Lambda - \Theta(\bar{y})\cos\Lambda - \frac{dW(\bar{y})}{d\bar{y}}\sin\Lambda + \sum_{i=1}^{N}\frac{\partial\alpha}{\partial\delta_i}\delta_i(y_h)\cos\Lambda_h \quad (10)$$

where α is the geometric angle of attack of the wing section about the pitch axis y, α_i is the induced angle of attack due to the downwash about the pitch axis y, γ is the wing pre-twist angle about the elastic axis $\bar{y} = y/\cos\Lambda$ (positive nose down), Θ is the wing torsional twist about the elastic axis $\bar{y}$ (positive nose down), W is wing vertical bending along the elastic axis (positive upward), Λ is the sweep angle of the elastic axis, and δ_i is the absolute deflection of the i-th flap segment of the VCCTEF about the hinge axis y_h which has a sweep angle of Λ_h.

Consider the lift circulation resulting from an off-design flight condition

$$\Gamma(y) = \frac{1}{2}V_\infty\left[C_l(y) + \Delta C_l(y)\right]c(y) \quad (11)$$

where $C_l(y)$ is the design lift coefficient distribution and $\Delta C_l(y)$ is the incremental lift coefficient distribution at off-design.

This can also be expressed as a Fourier sine series

$$\Gamma(\theta) = 2bV_\infty\sum_{n=1}^{N}(A_n + \Delta A_n)\sin n\theta \quad (12)$$

where ΔA_n is the incremental Fourier series coefficient due to the incremental lift coefficient ΔC_l which

is influenced by aeroelasticity according to

$$\Delta C_l\left(y\right) = C_{l_\alpha}\left[\Delta\alpha - \alpha_i\left(y\right) - \Delta\Theta\left(\bar{y}\right)\cos\Lambda - \frac{d\Delta W\left(\bar{y}\right)}{d\bar{y}}\sin\Lambda + \sum_{i=1}^{N}\frac{\partial\alpha}{\partial\delta_i}\Delta\delta_i\left(y_h\right)\cos\Lambda_h\right] \quad (13)$$

where Δ denotes the change in the variable.

The wing lift coefficient is given by $C_L = A_1\pi AR$ where AR is the wing aspect ratio. Also, the wing incremental lift coefficient is given by $\Delta C_L = \Delta A_1\pi AR$. The induced drag is computed as

$$C_{D_i} = \left(A_1 + \Delta A_1\right)^2\pi AR\times \times\left[1 + \sum_{n=2}^{N} n\left(\frac{A_n + \Delta A_n}{A_1 + \Delta A_1}\right)^2\right] = \frac{\left(C_L + \Delta C_L\right)^2}{\pi AR\left(e + \Delta e\right)} = \frac{\left(C_L + \Delta C_L\right)^2}{\pi ARe} + \frac{2C_L\Delta C_L}{\pi ARe_1} + \frac{\Delta C_L^2}{\pi ARe_2} \quad (14)$$

where e is the design span efficiency factor, Δe is the incremental span efficiency factor at off-design, and e_1 and e_2 are span efficiency factors associated with ΔC_L which are given by

$$\frac{1}{e} = 1 + \sum_{n=2}^{N} n\left(\frac{A_n}{A_1}\right)^2 \quad (15)$$

$$\frac{1}{e_1} = \sum_{n=2}^{\infty} n\left(\frac{A_n}{A_1}\right)\left(\frac{\Delta A_n}{\Delta A_1} - \frac{A_n}{A_1}\right) \quad (16)$$

$$\frac{1}{e_2} = \sum_{n=2}^{N} n\left[\left(\frac{\Delta A_n}{\Delta A_1}\right)^2 - \left(\frac{A_n}{A_1}\right)^2\right] \quad (17)$$

The contributions to the induced drag by the last two terms in Eq. (14) represent the induced drag penalty, which can be minimized by the VCCTEF. If the induced drag penalty is ideally reduced to zero, this would result in

$$\Delta A_n = \frac{\Delta C_L}{C_L}A_n \quad (18)$$

which can be used to determine the theoretical VCCTEF deflections along the wing span to achieve the design span efficiency factor.

The analysis is intended to illustrate the induced drag penalty due to the aeroelastic deflections. In practice, an aero-structural optimization study is conducted to determine the optimal VCCTEF settings to achieve a minimum drag for the flexible wing GTM [14, 15, 16]. An aeroelastic model is developed using a NASA vortex-lattice code, VORLAX, coupled with a finite-element model (FEM) code [17] and a 2D transonic small disturbance code TSFOIL2 for transonic correction [18]. Skin friction drag is added to partially correct for viscous drag contribution. The modeling environment has an automated mesh generation capability to modify the vortex-lattice mesh to account for aeroelastic deflections computed by the FEM code and the VCCTEF settings determined by the optimizer [17, 19]. In addition, a higher-fidelity Euler CFD model is also developed for the optimization using CART3D tool [20]. A RANS CFD capability is being developed to enable high-fidelity CFD assessments with full viscous effects in the near future.

The design cruise lift coefficient for the baseline GTM is selected to be 0.51 corresponding to a mid-cruise point with a gross weight of 210,000 lbs at Mach 0.797 and altitude of 36,000 ft. The half-stiffness wing GTM at the mid-cruise has a gross weight of 204,636 lb. The weight reduction is attributed to the reduced structural weight of the wings. The mid-cruise point corresponds to a 50% fuel loading. The off-design cruise flight conditions include a beginning cruise condition at 80% fuel loading, an ending cruise condition at 20% fuel loading, a high-altitude cruise at 30% over the design cruise lift condition, and a low-altitude cruise at 30% under the design cruise lift condition. The 30% over-design C_L cruise conditions correspond to altitude of about 41,500 ft which could exceed the aerodynamic ceiling since engine thrust requirement is not accounted for.

Table 3: GTM Off-Design Cruise Conditions

	Gross Weight, lbs	Altitude, ft	Cruise C_L
Baseline Stiffness Wing GTM, 20% Fuel	187,500	36,000	0.5099
Baseline Stiffness Wing GTM, 50% Fuel	210,000	36,000	0.4553
Baseline Stiffness Wing GTM, 80% Fuel	232,500	36,000	0.5645
Baseline Stiffness Wing GTM, 50% Fuel, 30% C_L Increase	210,000	41,458	0.6628
Baseline Stiffness Wing GTM, 50% Fuel, 30% C_L Decrease	210,000	28,312	0.3569
Half Stiffness Wing GTM, 20% Fuel	182,136	36,000	0.4422
Half Stiffness Wing GTM, 50% Fuel	204,636	36,000	0.4969
Half Stiffness Wing GTM, 80% Fuel	227,136	36,000	0.5515
Half Stiffness Wing GTM, 50% Fuel, 30% C_L Increase	204,636	41,464	0.6460
Half Stiffness Wing GTM, 50% Fuel, 30% C_L Decrease	204,636	28,317	0.3478

A jig-shape twist optimization is performed for a wing-body GTM configuration at the design mid-cruise condition to attain an aerodynamically optimal jig-shape wing design corresponding to the baseline stiffness and half stiffness wings. Figures 15 and 16 show the lift distributions with the jig-shape twist and optimized twist for the baseline stiffness wing and half stiffness

wing, respectively. The twist optimization results in a drag reduction of 0.00011 or 2.6% for the baseline stiffness wing and 0.00026 or 5.6% for the half stiffness wing. The span load for the half stiffness wing substantially deviates from the ideal elliptical lift distribution, whereas the span load for the baseline stiffness wing more or less resembles the elliptical lift distribution. Upon twist optimization, both span loads follow nearly the elliptical lift distribution particularly in the outboard wing area.

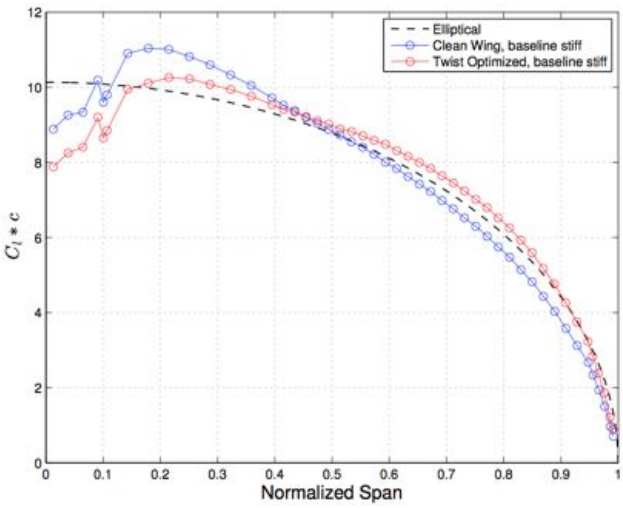

Figure 15: Optimized Span Loads of Baseline Stiffness Wing at Mid-Cruise Condition Computed by Coupled VORLAX-FEM

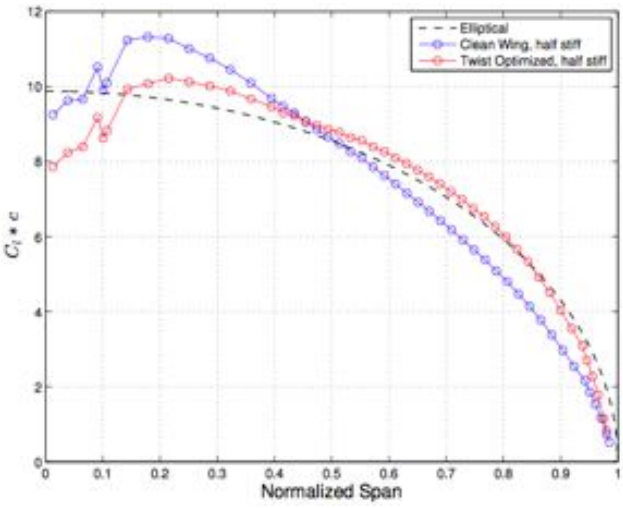

Figure 16: Optimized Span Loads of Half Stiffness Wing at Mid-Cruise Condition Computed by Coupled VORLAX-FEM

The wing-body GTM configurations for the baseline stiffness and half stiffness wings with the corresponding optimized twists are then used for evaluating the effectiveness of the VCCTEF at off-design cruise conditions. A drag optimization is conducted for the VCCTEF layout as shown in Figure 9. The individual VCCTEF deflection is described by a Chebyshev cubic polynomial. Thus, the polynomial coefficients are the design variables in the drag optimization. A relative deflection constraint of 2° is imposed on the deflections of any two adjacent spanwise flap sections. The chordwise flap segments are deflected in the circular arc fashion. The results for the drag optimization are shown in Table 4. The trend in the optimization results indicates that the VCCTEF achieves more drag reduction as the cruise C_L increases. For the 30% over-design C_L cruise condition, a drag reduction of more than 4% is obtained from the optimization. It is thought that the half stiffness wing is more flexible, therefore would allow more effective adaptive aeroelastic wing shaping control to achieve greater drag reduction. However, this is not evident from the optimization results which indicate about the same percentage drag reduction for the baseline stiffness wing and half stiffness wing.

Table 4: VCCTEF Drag Optimization Results Computed by Coupled VORLAX-FEM

	C_D Clean Wing	C_D Optimized VCCTEF	C_D Reduction
Baseline Stiffness Wing Optimized Twist, 20% Fuel	0.01938	0.01919	1.0%
Baseline Stiffness Wing Optimized Twist, 80% Fuel	0.02433	0.02371	2.6%
Baseline Stiffness Wing Optimized Twist, 30% c_L Decrease	0.01553	0.01548	0.3%
Baseline Stiffness Wing Optimized Twist, 30% c_L Increase	0.03049	0.02909	4.6%
Half Stiffness Wing Optimized Twist, 20% Fuel	0.01903	0.01881	1.2%
Half Stiffness Wing Optimized Twist, 80% Fuel	0.02397	0.02340	2.4%
Half Stiffness Wing Optimized Twist, 30% c_L Decrease	0.01536	0.01528	0.5%
Half Stiffness Wing Optimized Twist, 30% c_L Increase	0.02975	0.02847	4.3%

Figures 17 and 18 show an optimized VCCTEF deflection and the corresponding lift distribution for the 30% over-design C_L cruise condition. The absolute flap deflection of the trailing edge flap segment ranges from 8° for flap section 1 at the wing root to 5° for flap section 13 near the outboard wing area. The span load for the half stiffness wing at 30% over-design C_L cruise condition with the optimized VCCTEF does not follow the elliptical lift distribution as well as the span load for the clean wing with only optimized twist. This perhaps could be due to the fuselage-wing interference effect that causes the fuselage lift to decrease while the wing lift to increase as a result of the change in the trim angle of attack from 3.35° for the clean wing

to $0.5°$ for the optimized VCCTEF.

It should be noted that the optimization results may only be local minimum solutions. An exhaustive search has not been conducted to identify other possible local minimum solutions or perhaps global minimum solutions. An integral boundary layer method is being developed to provide better estimates of viscous drag. Optimization will be re-conducted with the improved viscous drag model. A similar drag optimization study has been conducted in CART3D and confirms the effectiveness of the VCCTEF in drag reduction [16]. Other VCCTEF studies have been conducted by other researchers for the Common Research Model (CRM) [21] and Truss-Braced Wing (TBW) [22] configurations and also indicate potential drag reduction benefits of the VCCTEF.

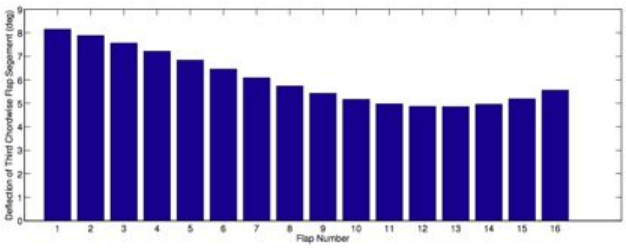

Figure 17: Optimized VCCTEF Deflection for Half Stiffness Wing at 30% Over-Design C_L Cruise Condition Computed by Coupled VORLAX-FEM

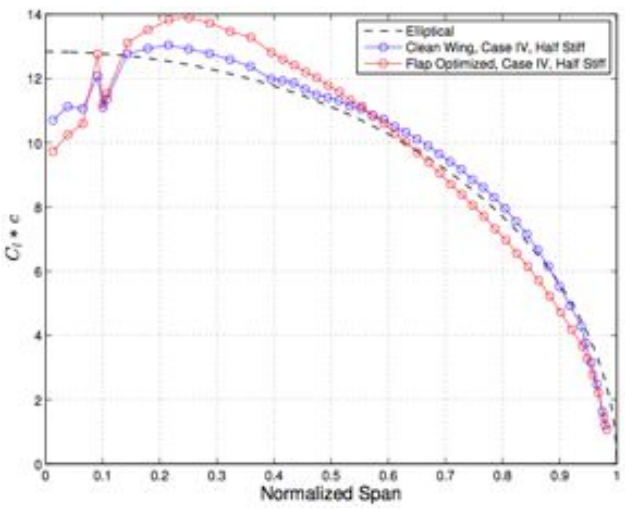

Figure 18: Optimized Span Loads of Half Stiffness Wing at 30% Over-Design C_L Cruise Condition Computed by Coupled VORLAX-FEM

To better explore the potential benefits of the VCCTEF, trade studies of different numbers of chordwise flap segments and spanwise flap sections and the camber shapes besides the circular arc camber will also need to be investigated by conducting drag optimization to identify possible improved design candidates. In addition, aeroelastic tailoring and active control design for load alleviation [22, 23] and flutter suppression [24] could also be included in the trade studies to minimize the structural weight which would lead to a reduction in the trimmed drag.

5 WIND TUNNEL TESTS

A series of two wind tunnel tests were performed in the Kirsten wind tunnel at the University of Washington (UWAL) to explore the relative merits of the VCCTEF as a cruise drag reduction wing shaping control device and a high-lift device. The first test entry in August of 2013 was designed as an exploratory test to measure the drag reduction benefit of the VCCTEF [9, 10]. The second test entry in July of 2014 was designed to assess the high-lift performance of the VCCTEF [11, 12].

5.1 CRUISE CONFIGURATION TEST The test article for the cruise configuration test is a 10%-scaled aeroelastic model of a flexible GTM wing. The semi-span of the model is 73.29 inches, as shown in Figure 19.

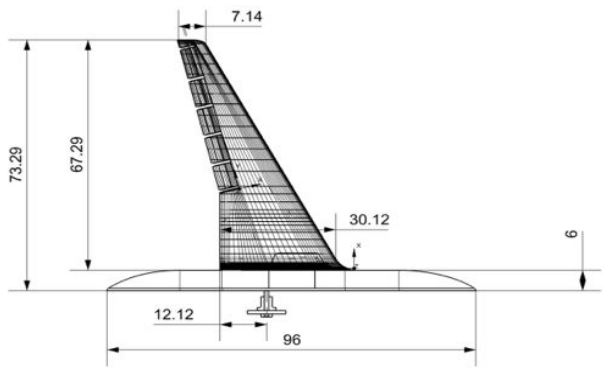

Figure 19: UWAL Wind Tunnel Model with VCCTEF (Courtesy of University of Washington Aeronautical Laboratory)

The model is constructed of woven fabric composites skin and extruded polystyrene foam core. The composite laminates and extruded polystyrene foam core are structurally tailored to attain half of the bending stiffness of the scaled baseline GTM wing stiffness while keeping torsional stiffness about the same. This tailored stiffness is to achieve a 10% wing tip deflection. The flap segments are mechanically interlocking aerodynamic surfaces in the chordwise direction and inter-connected by a silicone elastomer material in

between the spanwise flap sections, as shown in Figure 20. The flap segments are hinged at three chordwise locations and are designed to be fully adjustable. The UWAL aeroelastic wind tunnel model was built with a different stiffness than the scaled baseline GTM wing. The same jig shape as that of the baseline non-optimized GTM wing was used. Therefore, the washout twist is non-optimal for the model when it operates at the design lift coefficient of 0.51.

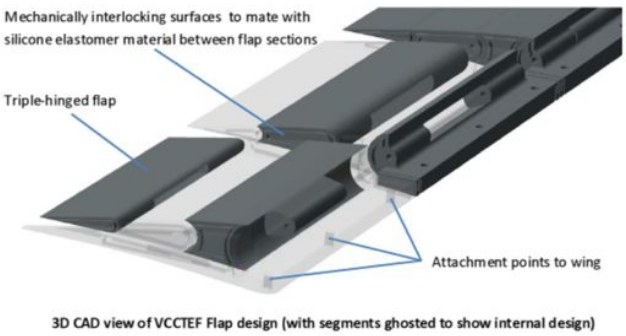

Figure 20: VCCTEF Construction (Courtesy of University of Washington Aeronautical Laboratory)

Figure 21 shows an exploded view of the UWAL wind tunnel model of the flexible wing mated to a center body fairing attached to an external floor-mounted balance.

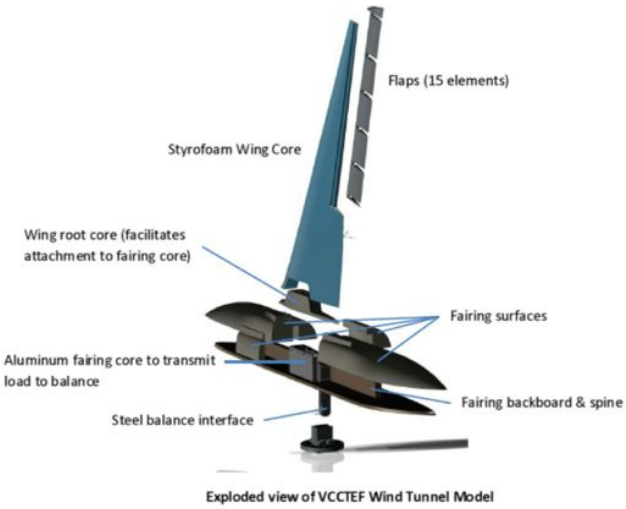

Figure 21: Exploded View of Wind Tunnel Model (Courtesy of University of Washington Aeronautical Laboratory)

The relevant model scaling information is given in Table 5. The test was conducted at a nominal dynamic pressure of 20 psf. Off-condition data and additional runs at 10, 15, 25 and 30 psf were also collected for some cases. The nominal test section airspeed was Mach 0.1162. Test data consist of force, moment, and aeroelastic deflection measurements, and were collected during α-sweep and q_∞-sweep runs. The aeroelastic deflection measurements were provided by a VICON motion tracking system. Figure 22 is a photograph of the flexible wing wind tunnel model in the UWAL test section during the cruise configuration test in 2013.

Table 5: UWAL Model Parameters

	Full-Scale	Semi-Span Model
M_∞	0.797	0.1162
C_L	0.51	0.51
h, ft	36,000	0
q_∞, psf	211.09	20.00
$S/2$, ft^2	975.5	9.638
$\bar{c}$, ft	16.6417	1.5963
$b/2$, ft	62.4167	6.1262

Figure 22: Flexible Wing Wind Tunnel Model in UWAL Test Section (Courtesy of University of Washington Aeronautical Laboratory)

The wind tunnel model was tested with a total of 13 VCCTEF configurations ranging from zero to full deflection. These VCCTEF configurations are designated as:

- FLAP0 - baseline zero deflection
- FLAP1 - full deflection for all flap sections
- FLAP2 - varying from a maximum deflection at the inboard and outboard flaps to a minimum deflection at the mid-span flap
- FLAP3 - varying from a minimum deflection at the inboard and outboard flaps to a maximum deflection at the mid-span flap

- FLAP4 - varying monotonically from a maximum deflection at the inboard flap to zero deflection at the outboard flap
- FLAP5 - varying monotonically from zero deflection at the inboard flap to a maximum deflection at the outboard flap
- FLAP6 - similar to FLAP4 configuration but with a smaller deflection
- FLAP7 - varying monotonically from a maximum positive deflection at the inboard flap to a negative deflection at the outboard flap
- FLAP8 - rigid-body deflection with the two outer camber segments at zero relative deflection
- FLAP9 - deflection of the trailing edge camber segments
- FLAP10 - intermediate deflection
- FLAP11 - full negative deflection
- FLAP12 - FLAP6 configuration plus a gurney flap

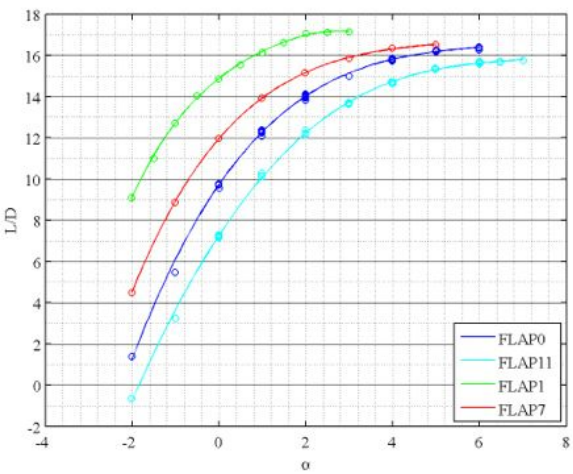

Figure 23: Lift-to-Drag Ratios for Selected VCCTEF Configurations in UWAL Cruise Configuration Test

Figure 23 is the plot of L/D for FLAP0, FLAP1, FLAP7, and FLAP11 configurations [10]. The baseline FLAP0 configuration has a L/D value of about 16.1 at $C_L = 0.51$. FLAP1 configuration has the highest L/D at the same C_L as compared to all the other VCCTEF configurations. Its L/D is about 17.2 which is about a 6.31% improvement. FLAP11 configuration is not aerodynamically efficient since it is configured as a lift-reduction device with negative VCCTEF deflections. Figure 24 shows the percentage drag reduction for all the VCCTEF configurations. FLAP 1 configuration achieves the largest drag reduction with 6.31% at the design cruise C_L. All VCCTEF configurations except FLAP11 and FLAP12 achieve varying degree of drag reduction.

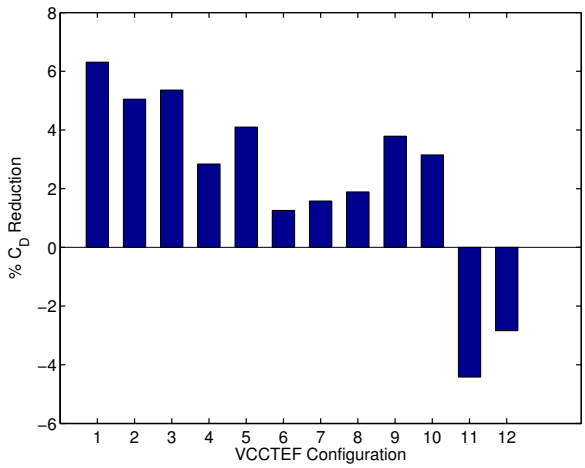

Figure 24: Drag Reduction of VCCTEF Configurations in UWAL Cruise Configuration Test

Aeroelastic analysis shows that the lift coefficient of a flexible wing at low dynamic pressure can be expressed as a function of the angle of attack, dynamic pressure and aeroelastic deflections as [10]

$$C_L = C_L^* + (a_0 + a_\alpha \alpha + a_\delta \delta)\, q_\infty + (b_0 + b_\alpha \alpha + b_\delta \delta)\, q_\infty^2 + (c_0 + c_\alpha \alpha + c_\delta \delta)\, q_\infty^3 \quad (19)$$

where C_L^* is the rigid-wing lift coefficient and $a_{(0,\alpha,\delta)}$ are negative for swept back wings.

Figure 25 shows the lift coefficient sensitivity to the dynamic pressure. As the dynamic pressure increases, the lift coefficient decreases. By extrapolation of the data to $q_\infty = 0$, one can estimate the rigid wing lift coefficient. Both linear and cubic polynomial extrapolation were used to correct the flexible wing lift curves to obtain the rigid wing lift curves. The cubic polynomial method is supposed to yield more accurate estimates according to Eq. (19).

Aeroelastic deflection measurements were taken with a VICON motion tracking system. The VICON system uses 54 optical targets, called dots, to create a three-dimensional displacement of the wind tunnel model as it is loaded. The displacement measurements at these dots are reduced to the spanwise out-of-plane deflections and twists at six spanwise locations, as shown in Figure 26. Figure 27 shows the measured bending deflection about the elastic axis of FLAP0 configuration. The wash-out twist about the pitch axis

due to bending slope is plotted in Figure 28. The flexibility results in a wash-out twist of $3.5°$ nose down at the wing tip corresponding to an angle of attack of $6°$ for FLAP0 configuration. For comparison, the calculated torsional twist about the elastic axis at the wing tip is less than $0.5°$, as shown in Figure 29. This indicates that the wing is much more flexible in bending than in torsion and that the wash-out twist effect is primarily due to wing bending [10, 25].

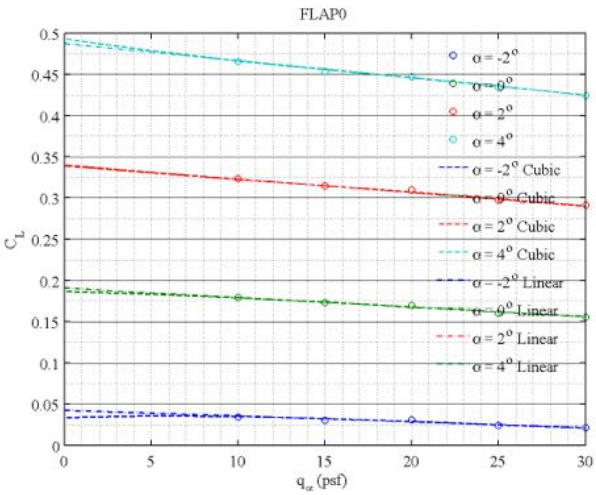

Figure 25: FLAP0 Cubic and Linear Variations of C_L with q_∞

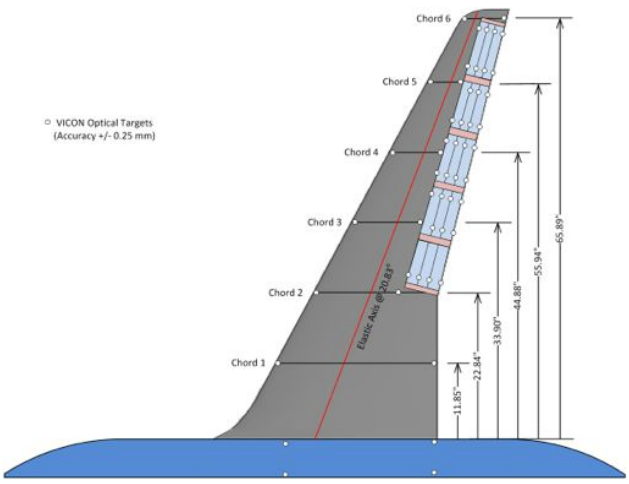

Figure 26: VICON Target and Spanwise Deflection Measurement Locations

As an alternative approach, the rigid wing lift coefficient can be estimated from the static bending and torsional deflections of the wing. The wing aeroelastic deflection results in an effective change in the angle of attack, which is computed as [10]

$$\Delta\alpha = -\frac{1}{C^*_{L_\alpha} S}\int_{-b/2}^{b/2} c^*_{L_\alpha}(y)\left[\Theta(\bar{y})\cos\Lambda + \frac{dW(\bar{y})}{d\bar{y}} w \sin\Lambda\right] c(y)\, dy \quad (20)$$

where $c^*_{L_\alpha}(y)$ is the sectional lift curve slope for the rigid wing.

This effective change in the angle of attack is a function of the angle of attack as

$$\Delta\alpha = \Delta\alpha_0 + \frac{\partial\Delta\alpha}{\partial\alpha}\alpha \quad (21)$$

By making an assumption that $c^*_{L_\alpha}(y) = C^*_{L_\alpha}$, the rigid wing lift coefficient can be computed from the flexible wing lift coefficient as [10]

$$C^*_L = C_L - \frac{C_{L_\alpha}\Delta\alpha}{1 + \frac{\partial\Delta\alpha}{\partial\alpha}} \quad (22)$$

Figure 30 shows the rigid wing lift coefficients estimated by the aeroelastic deflection correction method and the two q_∞-correction methods as compared to the flexible wing lift coefficient [10]. The aeroelastic deflection correction method yields the highest estimated rigid-wing lift coefficient. Since there are some differences in the three estimated rigid wing lift coefficients, an average rigid wing lift coefficient is computed and is shown in Figure 30. The q_∞-correction method by a cubic extrapolation perhaps might be more accurate than the aeroelastic deflection correction method which depends on the assumption of constant spanwise sectional lift curve slope that may not be realistic.

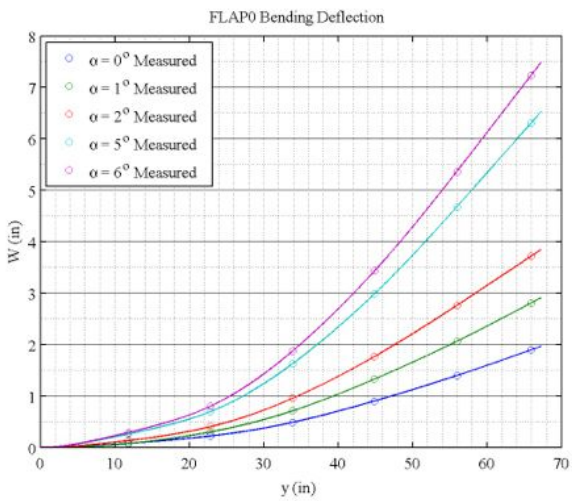

Figure 27: FLAP0 Bending Deflection

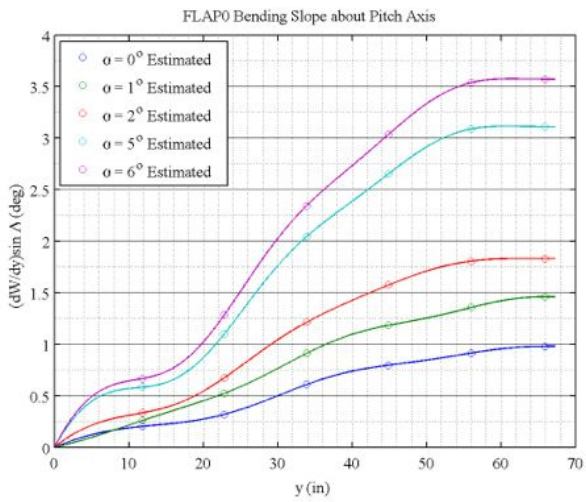

Figure 28: FLAP0 Bending Slope about Pitch Axis

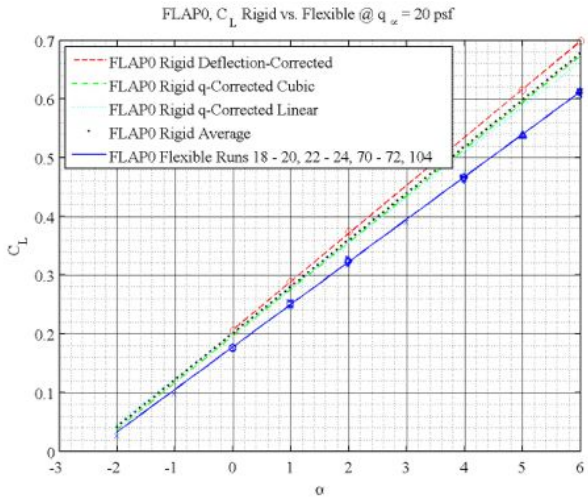

Figure 30: FLAP0 Measured C_L of Flexible Wing vs. Estimated C_L of Rigid Wing

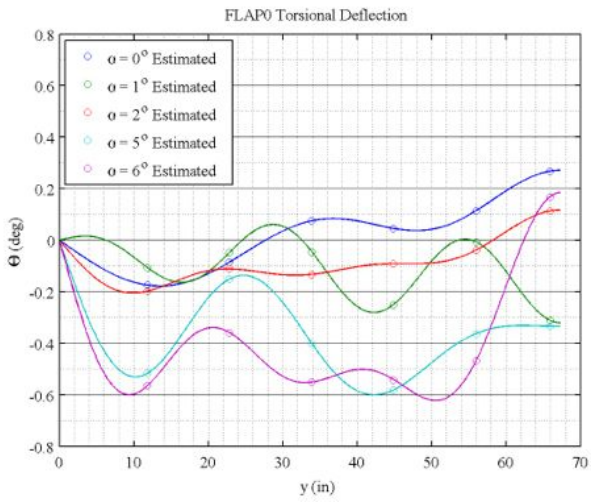

Figure 29: FLAP0 Torsional Twist about Elastic Axis

5.2 HIGH-LIFT CONFIGURATION TEST Typical high-lift flaps for transport aircraft use Fowler flap design in conjunction with the VCK to increase $C_{L_{max}}$. The Fowler motion requires flap track gearing mechanisms to translate the flap rearward to increase the effective wing surface area. These flap track mechanisms and the associated fairing covers can add a significant weight to the overall system weight. One option to simplify the high-lift system is to use the Fowler flap design only for the inboard high-lift flap. The outboard VCCTEF will not have the Fowler motion and instead will only rely on hinge-line actuation mechanisms provided by the SMA and electric actuators.

Figure 31 is a schematic of the high-lift wind tunnel model [11]. Figure 32 is an exploded view showing the component build-up of the wind tunnel model. Because of the structural flexibility, the VCK is fabricated in 12 individual sections with gap seals in between. The VCK sections are attached to the main wing structure by brackets as shown in Figure 33. Figure 34 shows the GTM wing wind tunnel model with high-lift flap deployed.

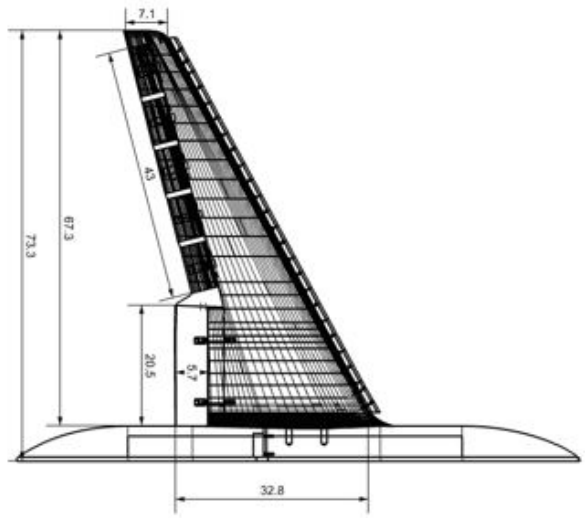

Figure 31: High-Lift Configuration of GTM Wing without High-Lift Flap (Courtesy of University of Washington Aeronautical Laboratory)

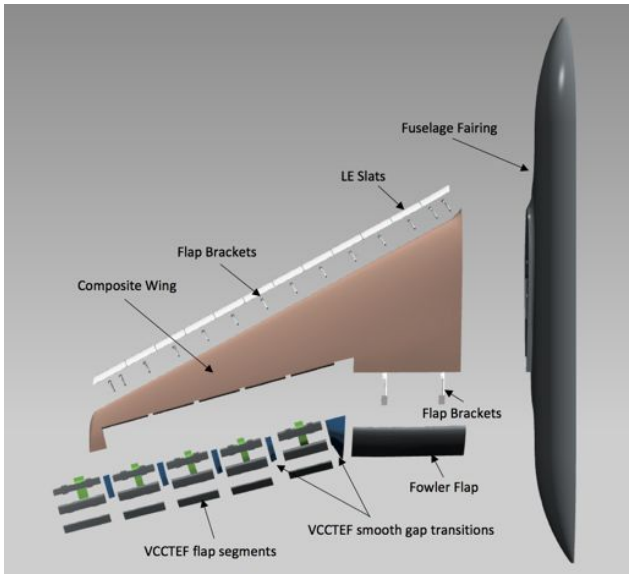

Figure 32: Exploded View of High-Lift GTM Wing (Courtesy of University of Washington Aeronautical Laboratory)

Figure 33: VCK Brackets (Courtesy of University of Washington Aeronautical Laboratory)

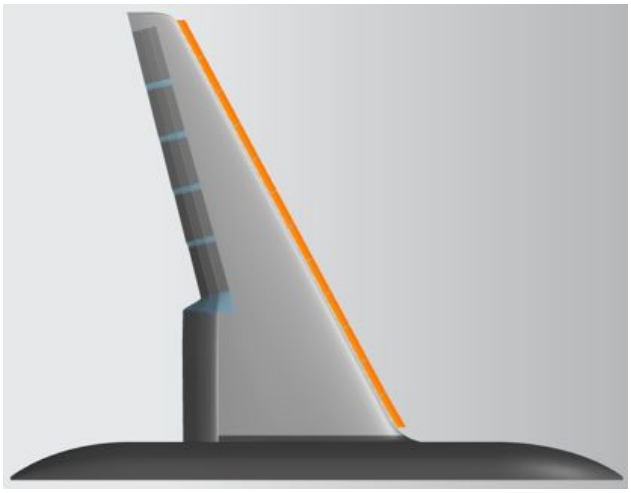

Figure 34: High-Lift Configuration with Flap Deployed (Courtesy of University of Washington Aeronautical Laboratory)

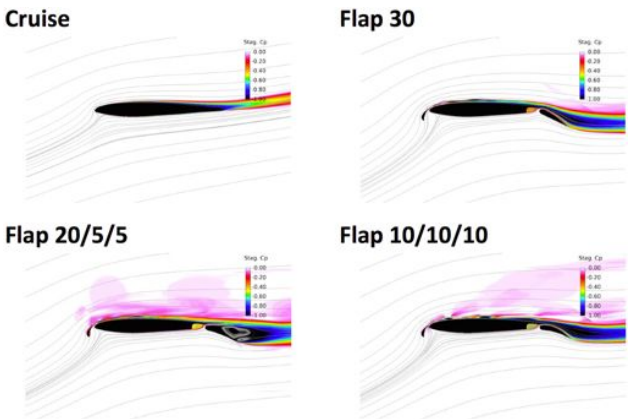

Figure 35: OVERFLOW 2D CFD Stagnation C_p Result at $\alpha = 14°$ with VCK Rigging Angle $65°$

The VCK sections are rigged at an angle of $65°$ based on an OVERFLOW 2D steady RANS CFD analysis, which shows that the VCK rigged at $65°$ provides a much better attached flow at the wing leading edge than if rigged at $55°$. The CFD analysis also examines three different high-lift flap configuration: 1) a single-element plain flap at $30°$ deflection, 2) a three-segment cambered flap at $20°/5°/5°$ deflection, and 3) a three-segment cambered flap at $10°/10°/10°$ deflection. The OVERFLOW results for the three different high-lift flap configurations indicate a significant flow separation associated with the cambered flaps, as shown in Figure 35 [12]. Thus, the baseline high-lift configuration is selected to be one with the VCK rigged at $65°$ and the single-element plain flap at $30°$ deflection. In addition to the single-element plain flap, the cambered flap at $10°/10°/10°$ deflection is also fabricated and tested. It should be noted that the 2D

lift prediction in general is more conservative than a 3D lift prediction.

The test was conducted at a nominal dynamic pressure of about 6 psf to limit the balance loads. Figure 36 is a photograph of the high-lift wind tunnel model in the UWAL test section.

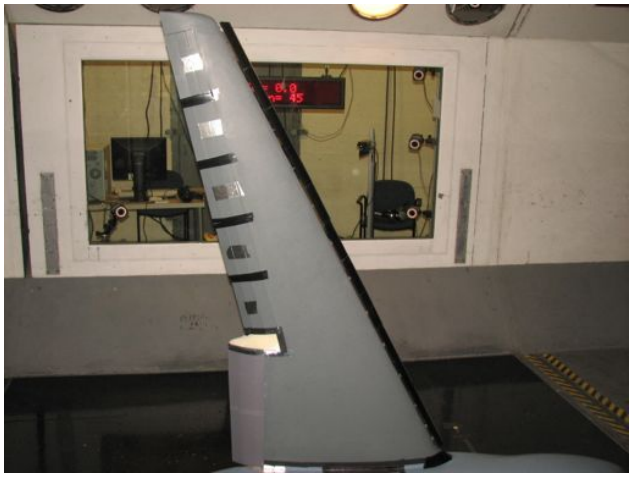

Figure 36: High-Lift Flexible Wing Wind Tunnel Model in UWAL Test Section (Courtesy of University of Washington Aeronautical Laboratory)

Several configurations were tested in various combinations which include three wing configurations, three inboard high-lift flap configurations, five outboard VCCTEF configurations, six VCK configurations, and four Fowler slot configurations. These configurations are designated as [12]

- W2.0 - Clean wing
- W2.1 - Wing with vortex generators (VG's) placed 1 inch aft of wing leading edge and spaced 6 inches between pairs.
- W2.2 - Wing with trip dots placed 0.5 inch back from wing leading edge.
- HLF0 - inboard high-lift plain flap with $0°$ deflection.
- HLF1 - inboard high-lift plain flap with $30°$ deflection.
- HLF2 - inboard high-lift three-segment cambered flap with $10°/10°/10°$ deflection, where the individual flap deflections are defined relative to the forward wing or chordwise flap segment.
- VCK - Baseline VCK rigged at $65°$.
- VCK1.1 - Baseline VCK with trip dots placed 1 inch from VCK leading edge.
- VCK1.2 - VCK with segments 8 to 12 rigged at a varying rigging angle from $65°$ to $60.5°$.
- VCK1.3 - VCK with segments 8 to 12 rigged at $50°$.
- VCK1.4 - VCK with segments 8 to 12 rigged at $50°$ and segments 5 to 7 rigged at $57.5°$. In addition, the VCK slot width varies from segment 1 to 12 with values 0.350, 0.300, 0.350, 0.352, 0.251, 0.253, 0.205, 0.253, 0.254, 0.205, 0.200, and 0.253 inch.
- VCK1.5 - VCK1.1 configuration with VCK 3/8-inch trailing edge extension for outboard 10.75-inch of VCK.
- FLAP0 - VCCTEF deflections are set at $(0°, 0°, 0°)$ for all flap sections.
- FLAP1 - VCCTEF deflections are set at $(10°, 10°, 10°)$ for all flap sections.
- FLAP2 - VCCTEF deflections are set at $(10°, 10°, 10°)$ for flap section 1, $(10°, 10°, 10°)$ for flap section 2, $(10°, 10°, 10°)$ for flap section 3, $(8°, 8°, 8°)$ for flap section 4, and $(4°, 4°, 4°)$ for flap section 5.
- FLAP3 - VCCTEF deflections are set at $(10°, 10°, 10°)$ for flap section 1, $(8°, 8°, 8°)$ for flap section 2, $(6°, 6°, 6°)$ for flap section 3, $(4°, 4°, 4°)$ for flap section 4, and $(2°, 2°, 2°)$ for flap section 5.
- FLAP4 - VCCTEF deflections are set at $(10°, 10°, 10°)$ for flap section 1, $(7°, 7°, 7°)$ for flap section 2, $(4°, 4°, 4°)$ for flap section 3, $(1°, 1°, 1°)$ for flap section 4, and $(-2°, -2°, -2°)$ for flap section 5.
- SLOT 0-4 - Fowler slot width 0 (SLOT0), 0.25 inch (SLOT1), 0.3 inch (SLOT2), 0.5 inch (SLOT3), and variable slot width from 0.3 inch at inboard to 0.1 inch at outboard of high lift flap (SLOT4).

There are a total of 58 test runs, of which the results from 44 runs were usable. The test run matrix is shown in Table 6.

The first ten runs were with the fuselage body alone. These runs are designated B1. Almost all of the high-lift test runs were conducted with the plain flap configuration HLF1. Runs 15 to 18 were designed to be repeat runs to compare with the clean wing data from the cruise configuration test in 2013. Runs 23 to 39 were exploratory runs to identify possible fixes to a premature stall of the baseline VCK configuration. Runs 40 to 58 are with the final configuration

with the VCK re-rigged to the proper rigging angles, designated as VCK1.4.

Table 6: UW2087 Test Run Matrix

Run Numbers	Configurations
3-9	B1
15-18	B1 + W2.0 + FLAP0
23, 24, 26	B1 + W2.0 + VCK + FLAP0
27	B1 + W2.1 + VCK + FLAP0
29, 30	B1 + W2.2 + VCK + HLF1 + FLAP4 + SLOT1
31-34, 36	B1 + W2.2 + VCK1.1 + HLF1 + FLAP4 + SLOT1
35	B1 + W2.2 + VCK1.5 + HLF1 + FLAP4 + SLOT1
37	B1 + W2.2 + VCK1.2 + HLF1 + FLAP4 + SLOT1
38	B1 + W2.2 + VCK1.3 + HLF1 + FLAP4 + SLOT1
39, 42	B1 + W2.2 + VCK1.4 + HLF1 + FLAP4 + SLOT1
40	B1 + W2.2 + VCK1.4 + HLF0 + FLAP0 + SLOT1
41	B1 + W2.2 + VCK1.4 + HLF1 + FLAP2 + SLOT1
43, 49, 50-55	B1 + W2.2 + VCK1.4 + HLF1 + FLAP1 + SLOT1
44	B1 + W2.2 + VCK1.4 + HLF1 + FLAP3 + SLOT1
45	B1 + W2.2 + VCK1.4 + HLF2 + FLAP4 + SLOT1
46	B1 + W2.2 + VCK1.4 + HLF1 + FLAP1 + SLOT4
47	B1 + W2.2 + VCK1.4 + HLF1 + FLAP1 + SLOT3
48	B1 + W2.2 + VCK1.4 + HLF1 + FLAP1 + SLOT2
56-58	B1 + W2.2 + VCK1.4 + HLF2 + FLAP1 + SLOT1

Initial shakedown test runs were conducted to verify the general lift characteristics of the high-lift wind tunnel model. Indications of flow anomaly were noticed as the angle of attack increased. Premature stall was noted on the lift curve. Tufts were then installed on the model for flow visualization which revealed aerodynamic issues with premature flow separation at the wing outboard due to incorrect rigging of the VCK. Subsequently, angled shims were made to readjust the VCK brackets [12]. The VCK inboard sections 1 to 4 were kept at their original rigging angle of $65°$. The VCK mid-sections 5 to 7 were readjusted to a rigging angle of $57.5°$. The VCK outboard sections 8 to 12 were readjusted to a rigging angle of $50°$. By adjusting the rigging angle of the VCK, high-lift aerodynamics of the model significantly improved. Figure 37 shows the lift curves for the clean wing with the VCK alone before and after the VCK rigging angle adjustment. Prior to the VCK rigging angle adjustment, the clean wing configuration with the baseline VCK reaches a stall angle of attack of $17°$ and a corresponding C_L of about 1.2. After the VCK rigging angle adjustment to the VCK1.4 configuration, the stall angle of attack increases to $22°$ corresponding to a $C_{L_{max}}$ of 1.7. Comparing the baseline VCK and the VCK1.4 configurations, it is evident that the VCK adjustment was highly effective in eliminating the premature flow separation due to the constant VCK rigging angle of $65°$ in the baseline VCK configuration. This incorrect rigging is due to the 2D CFD analysis of the inboard high-lift flap that did not account for the different flow characteristics in the wing outboard area which could be influenced by a number of factors including the aeroelastic effect, the absence of the Fowler slot, and the presence of the VCCTEF in lieu of the high-lift plain flap.

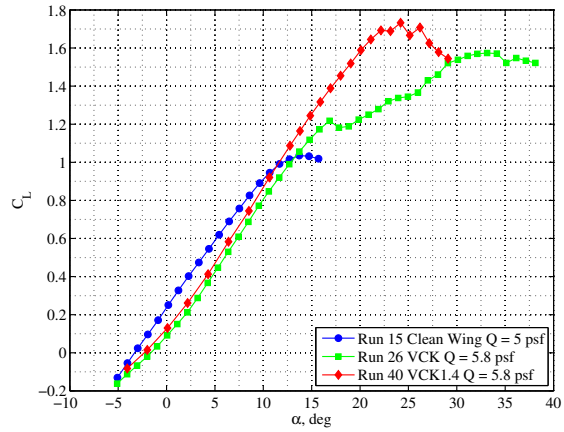

Figure 37: Lift Curve Before and After VCK Rigging Angle Adjustment

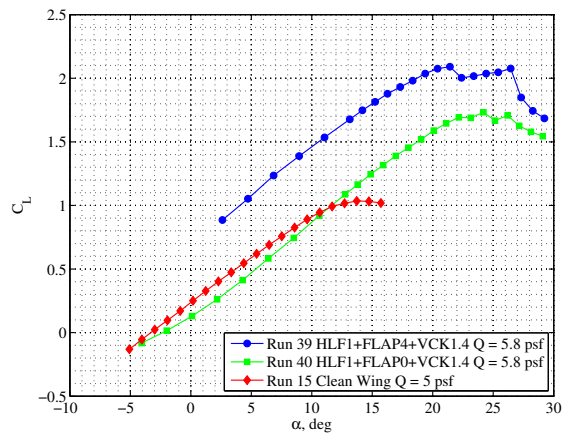

Figure 38: Lift Curves for Cruise Configuration, Cruise Configuration with VCK, and High-Lift Configuration

Because the high-lift test was conducted at a fairly low Reynolds number when a significant portion of the wing could be in the laminar boundary layer, trip dots were placed on the main wing very close to the leading edge in order to ensure fully turbulence flow over the main wing. Figure 38 shows the lift curves for the clean wing cruise configuration, the cruise configuration with the VCK deployed, and the high-lift configuration. The clean wing configuration achieves a $C_{L_{max}}$ of 1.05 at a stall angle of attack of $14°$. The

powerful effect of the VCK on the lift curve is noticed as the stall angle of attack increases from $14°$ to $22°$ which results in a $C_{L_{max}}$ of 1.7. With the VCK and the Fowler plain flap deployed in a high-lift configuration, the stall angle of attack reduces to $19°$ corresponding to a $C_{L_{max}}$ of 2.1. The reduction in the stall angle of attack as the trailing edge flap is deployed is consistent with the high-lift aerodynamics. The high-lift $C_{L_{max}}$ of 2.1 is close to the desired $C_{L_{max}}$ for a typical Boeing 757 landing configuration. Thus, the wind tunnel test data confirms that the high-lift design for the VCCTEF is capable of providing high-lift performance for transport aircraft [12].

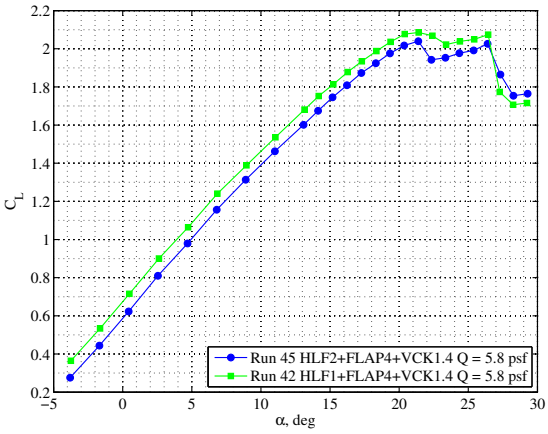

Figure 39: Lift Curves for Single-Element Plain Flap and Three-Segment Cambered Flap

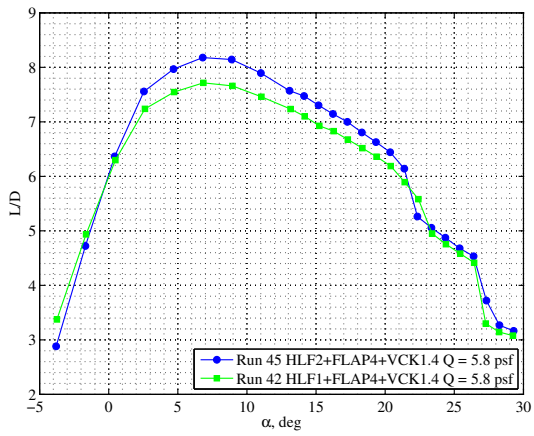

Figure 40: L/D for Single-Element Plain Flap and Three-Segment Variable Camber Flap

Figure 39 shows the lift curves for the single-element plain flap and the three-segment variable camber flap. The three-segment variable camber flap attains a slight lower $C_{L_{max}}$ of 2.05 than that for the single-element plain flap. This reduction in lift is consistent with the theoretical lift based on the potential flow theory discussed in Section 3. While the three-segment cambered flap results in a slight lift reduction, it significantly improves aerodynamic efficiency or L/D by about 6% over the single-element plain flap. This is shown in Figure 40. The wind tunnel test data thus confirms the drag reduction benefit of the three-segment cambered flap over the plain flap. Also, while the 2D OVERFLOW CFD predicts a significant flow separation associated with the three-segment cambered flap, this is not evident in the 3D wind tunnel test data.

The Reynolds number / aeroelastic effect was also investigated for both the plain flap and three-segment cambered flap configurations. It should be noted that, because the flexible wing wind tunnel model is an aeroelastic model with a significant wing aeroelastic deflection, there is really no “pure” Reynolds number effect. As the dynamic pressure changes, both the Reynolds number effect and aeroelastic effect act together to change lift. In general, $C_{L_{max}}$ increases with increasing the Reynolds number [26, 27] but decreases with increasing the dynamic pressure for a sweptback wing [10]. Figures 41 and 42 show the lift curves for the high-lift plain flap configuration at a varying dynamic pressure $q_\infty = 1$ psf to 5.8 psf. As the dynamic pressure, hence Reynolds number, increases, the skin friction coefficient decreases for a fully turbulent boundary layer [28]. As a result, viscous drag generally decreases while lift increases with increasing Reynolds number. The wind tunnel test data indicate that the Reynolds number effect outweighs the aeroelastic effect at stall. Otherwise, the trend of increasing $C_{L_{max}}$ with increasing the dynamic pressure would have been reversed. There is a marked change in the lift and drag characteristics at $\alpha = 11°$ for $q_\infty = 1$ psf, corresponding to a Reynolds number per unit length of 0.17906×10^6/ft, possibly indicating of a flow separation. At a dynamic pressure above 1 psf, the lift and drag characteristics appear similar.

Figure 43 shows a correlation of $C_{L_{max}}$ with the Reynolds number based on a power-rule formula [26, 27]

$$\frac{C_{L_{max}}}{C_{L_{max,ref}}} = \left(\frac{Re}{Re_{ref}}\right)^a \tag{23}$$

where Re is the Reynolds number based on the mean aerodynamic chord, and a is obtained from curve-fitting.

Using the data for $q_\infty = 2$, 3, 5, and 5.8 psf, the correlation results in $a = 0.0896624$. Reference [27] sug-

gests $a = 0.1$, which is in good agreement with the data.

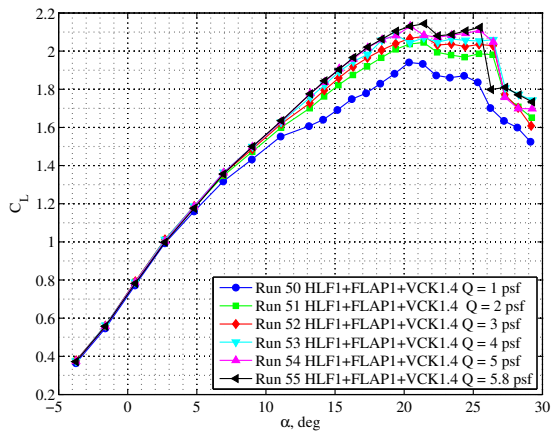

Figure 41: Reynolds Number / Aeroelastic Effect for Plain Flap on C_L

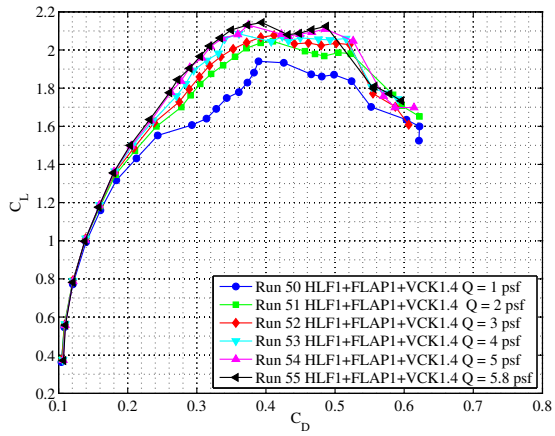

Figure 42: Reynolds Number / Aeroelastic Effect for Plain Flap on C_D

For a typical transport aircraft similar the Boeing 757, a typical approach speed is about 140 knots at sea level. Using a conservative 30% stall speed margin, the stall speed is about 108 knots. This correspond to a flight Reynolds number of 19.2048×10^6 based on the MAC of 16.6417 ft. The reference Reynolds number for $q_\infty = 2$ psf is 0.402416×10^6. Thus, if the power-rule correlation equation (23) is used for the Reynolds number correction, a 40% increase in $C_{L_{max}}$ would result. It is obvious that the Reynolds number correction using low Reynolds number data based on the power-rule correlation equation (23) is not reliable. Also the power-rule correlation equation (23) may be applicable for a "pure" Reynolds number correction, but for an aeroelastic model, this correction may result in an over-estimation of $C_{L_{max}}$ since the aeroelastic effect causes $C_{L_{max}}$ to decrease with increasing the dynamic pressure.

An alternative exponential correlation is sought based on an exponential function as

$$\frac{C_{L_{max}}}{C_{L_{max,ref}}} = a - be^{-c\left(\frac{Re}{Re_{ref}}\right)} \tag{24}$$

The correlation yields $a = 1.13063$, $b = 0.409968$, and $c = 1.14775$, as shown in Figure 44. Applying this correlation to the flight Reynolds number results in 13% increase in $C_{L_{max}}$ over the baseline $C_{L_{max}} = 1.9409$ at 1 psf, or $C_{L_{max}} = 2.1944$, which seems to be reasonable.

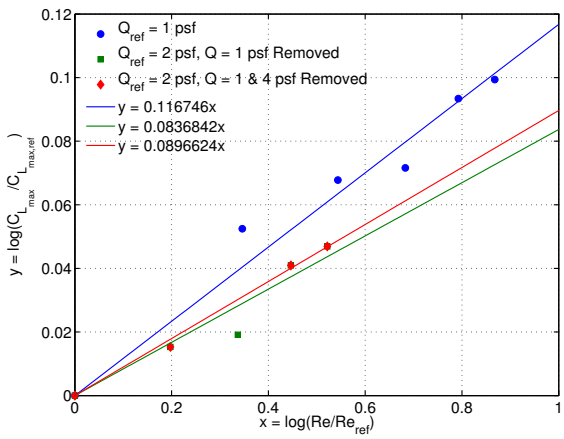

Figure 43: Power-Rule Correlation of $C_{L_{max}}$ with Reynolds Number

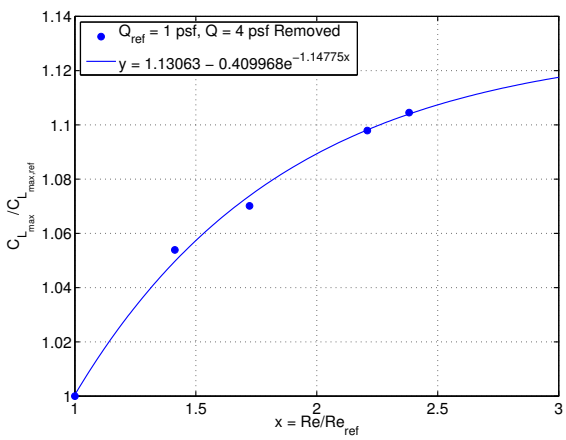

Figure 44: Exponential Correlation of $C_{L_{max}}$ with Reynolds Number

To correct for the Mach number effect, one can use the Prandtl-Glauert subsonic compressibility correction. This is only an approximate method since the flow at stall is nonlinear whereas the Prandtl-Glauert subsonic compressibility correction is applicable to linear subsonic flow. The Mach number correction factor also includes the effect of wing sweep. Thus

$$\frac{C_{L_{max}}}{C_{L_{max,ref}}} = \sqrt{\frac{1 - M_{\infty,ref}^2 \cos^2 \Lambda}{1 - M_\infty^2 \cos^2 \Lambda}} \tag{25}$$

where Λ is the sweep angle of the wing leading edge.

The stall speed is about Mach 0.16 whereas the reference speed is about Mach 0.03. For a sweep angle $\Lambda = 28°$, the Mach number correction results in 1% increase in $C_{L_{max}}$ or $C_{L_{max}} = 2.2169$ for the high-lift plain flap. Similar corrections for the Reynolds and Mach number effects are computed for the high-lift three-segment cambered flap and result in $C_{L_{max}} = 2.1927$ [12].

It should be noted that the $C_{L_{max}}$ correlation is for a wing with no engine nacelle and no horizontal tail. So, the $C_{L_{max}}$ estimate may not directly translate into a $C_{L_{max}}$ for a complete aircraft configuration. Nonetheless, this $C_{L_{max}}$ correlation can serve as a guide in the design of a high-lift system for a flexible wing transport similar to the high-lift configuration tested.

6 FLUTTER ANALYSIS AND SUPPRESSION CONTROL

6.1 FLUTTER ANALYSIS The flexibility of modern transport wings can cause a reduction in flutter margins which can compromise aircraft stability. A flexible wing is also more responsive to gust or maneuver loads which can lead to structural integrity issues as well as compromised ride and handling qualities. In the Phase II study, a flutter analysis was conducted to examine the effect of increased flexibility of the GTM wing on the flutter boundary [29]. The baseline stiffness of the GTM wing is reduced by 50% to create a flexible wing GTM with the goal of enabling more effective adaptive aeroelastic wing shaping control for improved aerodynamic efficiency. This half stiffness wing GTM is referred to as the Elastic Shaped Aircraft Concept (ESAC). Table 7 shows the flutter speed prediction at 35,000 ft for the GTM wing and the ESAC wing. The critical flutter modes for the GTM wing and ESAC wing are the first anti-symmetric bending mode. The flutter boundary for the ESAC wing is reduced by 31% as compared to the flutter boundary for the GTM wing. The flutter speed prediction is also compared against NASTRAN doublet lattice solution which gives a flutter speed of Mach 0.954 for the ESAC wing at 35,000 ft corresponding to the first anti-symmetric bending mode at a frequency of 2.53 Hz. Figures 45 to 48 show the frequencies and damping ratios for the anti-symmetric modes of the GTM wing and the ESAC wing [29].

Table 7: Flutter Speed Prediction

	Symmetric Mode	Anti-Symmetric Mode
GTM Wing Flutter Mach @ 35K ft	1.358	1.310
GTM Wing Flutter Frequency @ 35K ft, Hz	4.31	3.87
ESAC Wing Flutter Mach @ 35K ft	0.938	0.925
ESAC Wing Flutter Frequency @ 35K ft, Hz	6.94	2.85

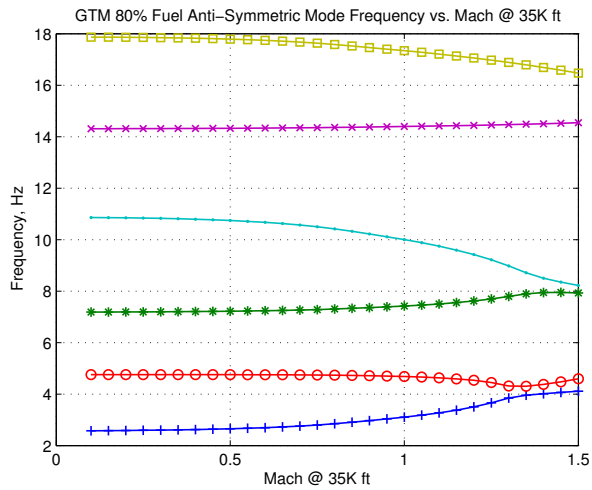

Figure 45: Frequencies of Anti-Symmetric Modes of GTM Wing

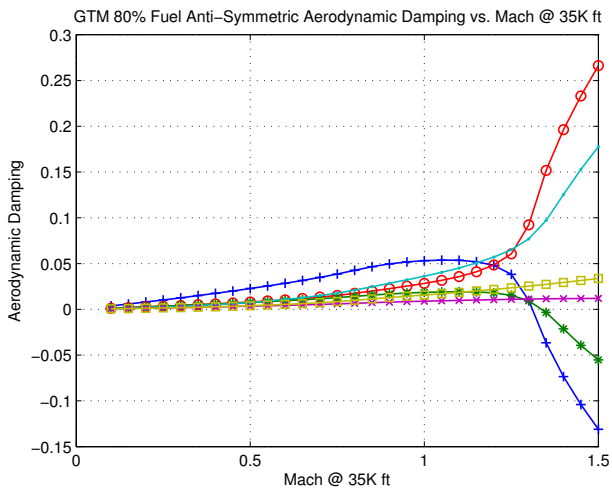

Figure 46: Damping Ratios of Anti-Symmetric Modes of GTM Wing

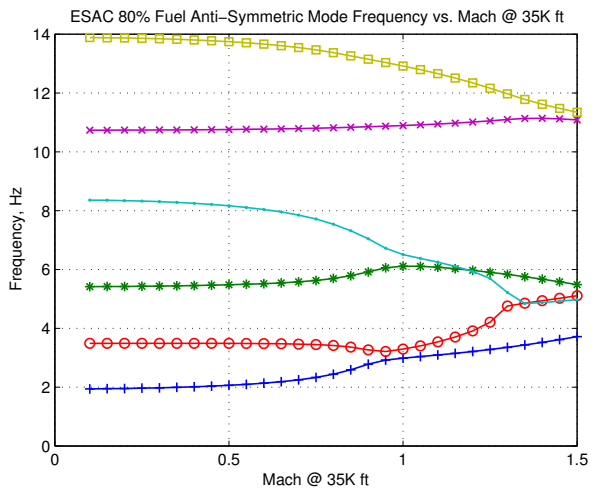

Figure 47: Frequencies of Anti-Symmetric Modes of ESAC Wing

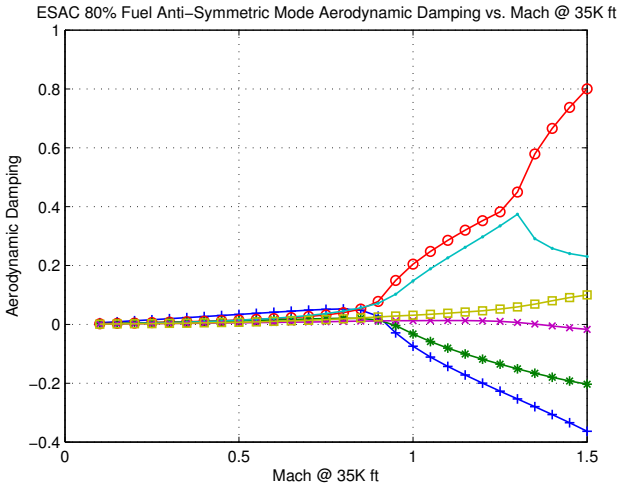

Figure 48: Damping Ratios of Anti-Symmetric Modes of ESAC Wing

A sensitivity study is conducted to determine the flutter boundary as a function of the ESAC wing torsional stiffness GJ while the ESAC wing bending stiffness EI is kept at half of that of the GTM wing. Figure 49 shows the flutter boundary for a varying torsional stiffness from 100% to 50% of that of the GTM wing. It can be seen that the flutter boundary is highly sensitive to the torsional stiffness. As GJ increases, the flutter boundary also increases. When GJ is at 100% of that of the GTM wing, the flutter speed of mode 1B is as high as that of the GTM wing. It should be noted that the bending stiffness is greater than the torsional stiffness for the GTM wing by a factor of almost 2:1. Therefore, if the torsional stiffness of the ESAC wing is kept the same as that of the GTM wing, then the bending stiffness and the torsional stiffness of the ESAC wing are about the same. This study shows that reducing the wing bending stiffness by no more than half while keeping the torsional stiffness the same as the conventional wing stiffness does not seem to significantly degrade the flutter boundary.

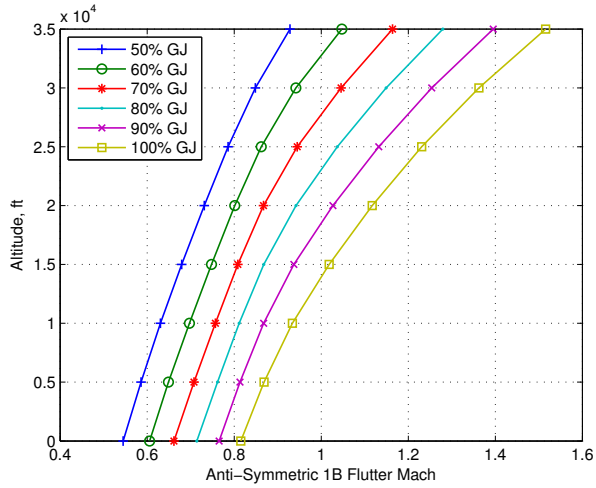

Figure 49: Flutter Boundary of ESAC Wing as a Function of GJ

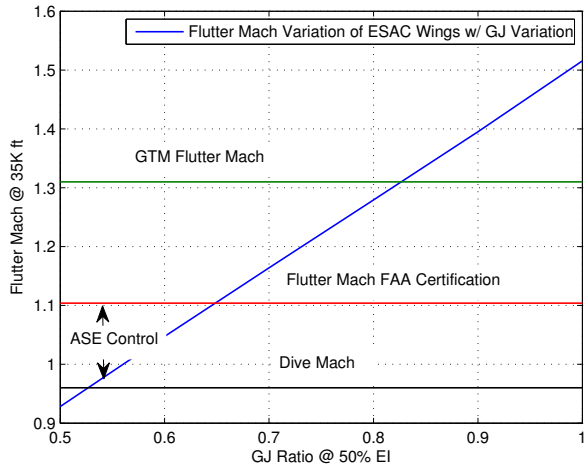

Figure 50: Flutter Speed Clearance of ESAC Wing

The FAA certification requires aircraft to demonstrate a flutter margin of at least 15% above the dive speed which is normally determined from flight testing. For a maximum operating Mach 0.8, the dive speed might be estimated at 20% over the maximum operating Mach. Thus, the flutter clearance would require the minimum flutter speed of at least Mach 1.1 at 35,000 ft. The GTM wing meets this flutter clearance but the ESAC wing does not if the torsional stiffness is re-

duced by half. As can be seen from Figure 50, to clear the flutter boundary at Mach 1.1, the ESAC wing torsional stiffness GJ cannot be reduced to less than 65% of that of the GTM wing. The question to be asked is whether or not there are any additional aerodynamic performance benefits by reducing the torsional stiffness GJ further in exchange for the need to incorporate active flutter suppression control. Currently, active flutter suppression has not been certified for transport aircraft, but this situation may change as the FAA has begun to investigate certification requirements for active flutter suppression control.

6.2 ADAPTIVE FLUTTER SUPPRESSION CONTROL Active flutter suppression control is a structural feedback control designed to suppress a flutter mode. The purpose of flutter suppression control is to increase the flutter speed of a flutter mode. An adaptive flutter suppression control is developed to demonstrate the feasibility of active flutter suppression for a highly flexible wing with a significantly degraded flutter margin [24].

The aeroservoelastic (ASE) state space model developed by Boeing in the Phase II study contains 22 aeroelastic modes and one rigid-body mode for a total of 45 states using the p-transform without unsteady aerodynamic lag states, 64 outputs, and 4 inputs. The states include one rigid-body state; namely the aircraft roll rate p, and two generalized states for each of the 22 aeroelastic modes. The outputs include the aircraft airspeed V_∞, angle of attack α, sideslip angle β, aircraft angular rates (p, q, r), aircraft position (x, y, z), aircraft attitude (ϕ, θ, ψ), accelerations in three axes (N_x, N_y, N_z) at forward of wing tip, aft of wing tip, wing root centerline, and engine center of gravity, and the four hinge moments of the control surfaces. The inputs are the four outboard third camber segments of the VCCTEF.

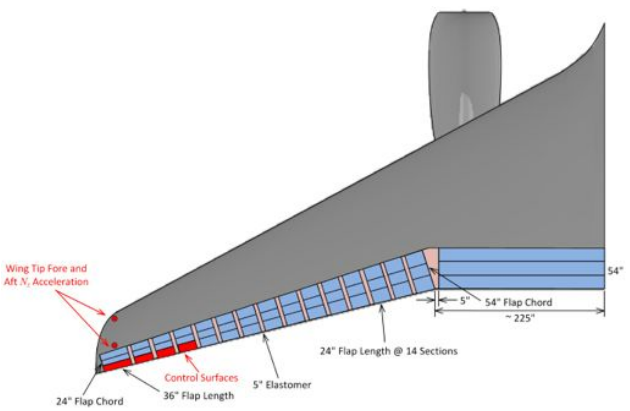

Figure 51: Flutter Suppression Input and Output Locations

For the flutter suppression control design, two N_z acceleration measurements are used as the outputs. Figure 51 illustrates the input and output locations.

All the control surfaces are not entirely independent in their motions due to the physical constraints imposed by the elastomer transition material. This material has certain position and rate limits. Thus, the control surfaces will have relative position and rate limits. These limits are not the normal position and rate limits that actuators are typically subjected to. Thus, these relative constraints can cause challenges in a control design of this system.

Consider the following relative constraints

$$|\delta_{i+1} - \delta_i| \leq \Delta\delta \tag{26}$$

$$\left|\dot{\delta}_{i+1} - \dot{\delta}_i\right| \leq \Delta\dot{\delta} \tag{27}$$

where $i = 1, 2, 3$.

For the VCCTEF design, the relative motion between any pair of adjacent flap sections is allowed to be within 2 degrees. The rate constraint imposed by the elastomer material is not yet defined and thus is assumed to be large. The actuator dynamics are modeled as a second-order system with a frequency of 9 Hz. This actuator model is highly simplified since it does not take into account the hinge moment which is a function of the states and the dynamics of the elastomer material which contributes mass, damping, and stiffness to the overall actuator model.

To address the relative position limit, a concept of virtual control has been introduced [4]. The control surface deflections are described by a shape function. This shape function can be any reasonable shape function with a smooth and gradual slope. One simple function is a linear function. The control surface deflections are then parametrized as a linear function

$$\delta_i = \frac{i\delta_v}{4} \tag{28}$$

where $i = 1, 2, 3, 4$ such that δ_1 is the inboard flap and δ_4 is the outboard flap, and δ_v is the virtual control surface deflection.

Since the inboard flap section δ_1 cannot deflect more than 2 degrees relative to the stationary flap adjacent to it, then $\delta_v \leq 8$ deg. Also, the outboard flap deflection δ_4 is the same as the virtual control surface deflection. Thus, one can think that outboard flap δ_4 is a master control input while the other three control surfaces are slave control inputs since their motions are dependent on the master control input.

Thus, the virtual control derivatives are computed as

$$B_{jk} = \sum_{i=1}^{4} \frac{iB_{jk_i}}{4} \tag{29}$$

where B_{jk_i} is the control derivative of mode j-th with respect to the displacement $(k = 1)$, velocity $(k = 2)$, and acceleration $(k = 3)$ of flap section i-th.

A model reduction is performed to reduce the number of states down to a manageable size. The model reduction approach is based on a singular perturbation method which eliminates high frequency modes and retains only all the lower frequency modes of interest including all the unstable modes. A reduced-order model that retains only the first 8 modes is found to match the full-order model very well. Table 8 shows the eigenvalues of the reduced-order model for a flight condition at Mach 0.86 and altitude of 10,000 ft for the half stiffness ESAC wing. The model exhibits two anti-symmetric flutter modes.

Table 8: Eigenvalues of Reduced-Order Model for Mach 0.86 and Altitude 10,000 ft

Mode	$n = 6$	$n = 7$	$n = 8$	$n = 22$ (Full)
Rigid	-2.7392	-2.7395	-2.7385	-2.7385
1	$2.7294 \pm 19.8683i$	$2.7512 \pm 19.8529i$	$2.7804 \pm 19.8561i$	$2.7842 \pm 19.8513i$
2	$-0.1553 \pm 24.3565i$	$-0.1557 \pm 24.3562i$	$-0.1547 \pm 24.3553i$	$-0.1549 \pm 24.3552i$
3	$-6.3434 \pm 24.0892i$	$-6.3272 \pm 24.0739i$	$-6.4220 \pm 23.9949i$	$-6.4174 \pm 23.9920i$
4	$-0.3902 \pm 37.1580i$	$-0.3782 \pm 37.1461i$	$0.0571 \pm 37.4423i$	$0.0584 \pm 37.4846i$
5	$-20.0160 \pm 32.3722i$	$-20.2813 \pm 32.3013i$	$-20.4217 \pm 32.4999i$	$-20.4833 \pm 32.5445i$

The ASE state space model is expressed in general as

$$\dot{x} = (A + \Delta A)\, x + (B + \Delta B)\, u \tag{30}$$

$$y = Cx + Du \tag{31}$$

where $\Delta A = \delta_A A$ and $\Delta B = \delta_B B$ are known perturbations of the A and B matrices, and δ_A and δ_B are assumed to be small parameters that represent multiplicative model variation due to uncertainty in the aeroelastic properties.

The linear quadratic gaussian (LQG) is a standard technique for control design of systems with output or partial state information. A state observer is constructed using the Kalman filter optimal estimation method as

$$\dot{\hat{x}} = A\hat{x} + L\,(y - \hat{y}) + Bu \tag{32}$$

where $\hat{x}$ is the estimated state vector, L is the Kalman filter gain, and $\hat{y}$ is the estimated output

$$\hat{y} = C\hat{x} + Du \tag{33}$$

The adaptive flutter suppression controller is designed as [24]

$$u = \bar{K}_x \hat{x} + u_{ad} \tag{34}$$

where $\bar{K}_x$ is obtained from the linear quadratic regulator (LQR) design of the full-state equation, and u_{ad} is an adaptive augmentation controller which is designed as

$$u_{ad} = \Delta K_x \hat{x} + K_y\,(y - \hat{y}) \tag{35}$$

The adaptive gains $\Delta K_x\,(t)$ and $K_y\,(t)$ are computed from the following adaptive laws:

$$\Delta \dot{K}_x^\top = -\Gamma_x \hat{x}\hat{x}^\top \left(P - \nu_x \Delta K_x^\top B^\top P A_m^{-1}\right) B \tag{36}$$

$$\dot{K}_y^\top = -\Gamma_y\,(y - \hat{y}) \left[\hat{x}^\top P - \nu_y\,(y - \hat{y})^\top K_y^\top B^\top P A_m^{-1}\right] B \tag{37}$$

The simulation is conducted with only the reduced-order aeroservoelastic state space model for flight condition at Mach 0.86 and altitude of 10,000 ft. There are two flutter modes: mode 1 and mode 4. Process noise and sensor noise are introduced to simulate the structural response to atmospheric turbulence. The baseline full-state feedback controller is designed with a LQR controller tuned to give good performance. A LQG output feedback controller is then designed using the ideal full-state feedback gain. The adaptive augmentation controller is then turned on. The adaptive gain matrices and modification parameters are selected to be $\Gamma_x = \Gamma_y = 1$ and $\eta_x = \eta_y = 0.1$.

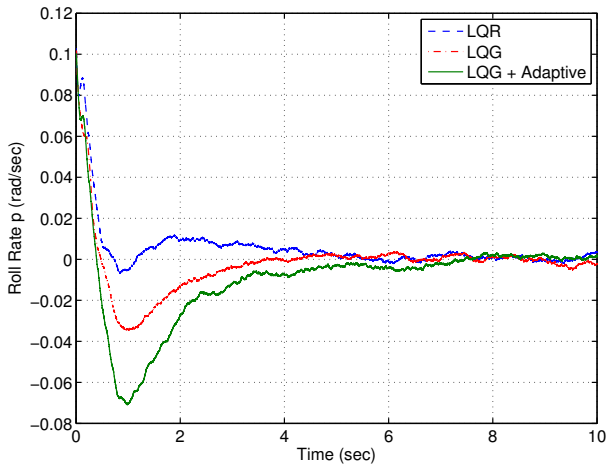

Figure 52: Roll Rate Response

An initial roll rate of 0.1 rad/sec is specified. Figures 52 to 54 show the responses of the roll rate, the generalized displacement of mode 1, and the

generalized displacement of mode 4 for the baseline full-state feedback LQR controller and the output feedback LQG controller with and without the adaptive augmentation controller. The full-state feedback LQR controller performs much better than the output feedback LQG controller with and without the adaptive augmentation controller using only the two accelerometers at the wing tip. The adaptive augmentation controller causes an increase in the overshoot of the responses due to the output feedback LQG controller as well as injects high frequency contents into the modal responses. Nonetheless, all the controllers are able to suppress the two flutter modes.

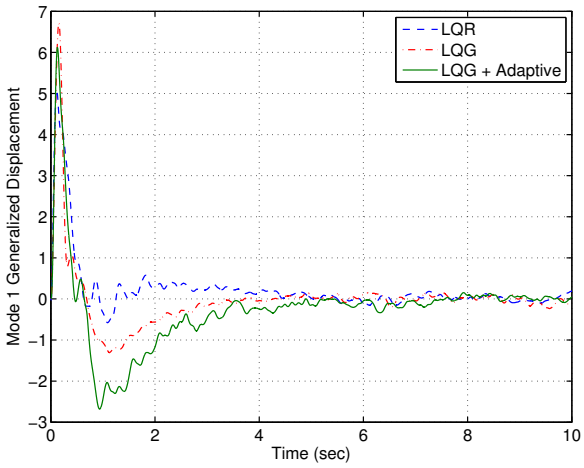

Figure 53: Mode 1 Generalized Displacement

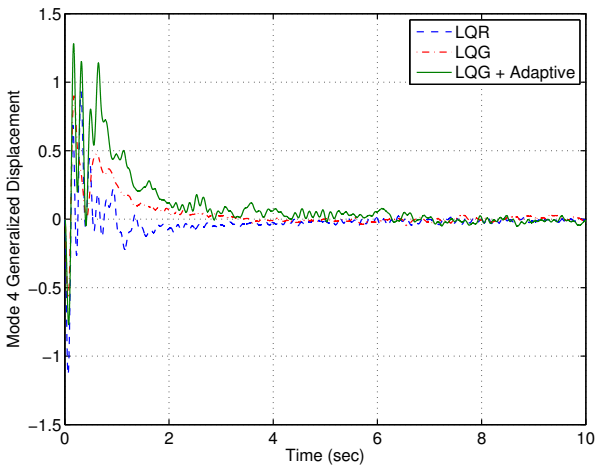

Figure 54: Mode 4 Generalized Displacement Response

Next, model variation is introduced into the aeroservoelastic state space model by $\Delta A = 0.05A$ and $\Delta B = -0.1B$. Process and sensor noises are also included. The output feedback LQG controller without the adaptive augmentation controller is unstable as shown in Figures 55 to 57. The adaptive augmentation controller is able to stabilize the flutter modes in the presence of the model variation.

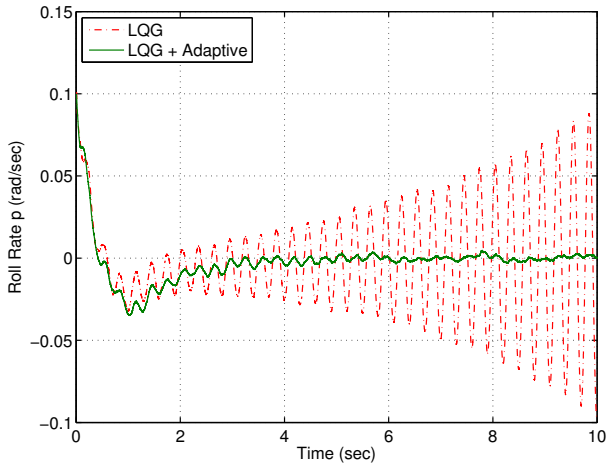

Figure 55: Roll Rate Response with and without Adaptive Augmentation Controller

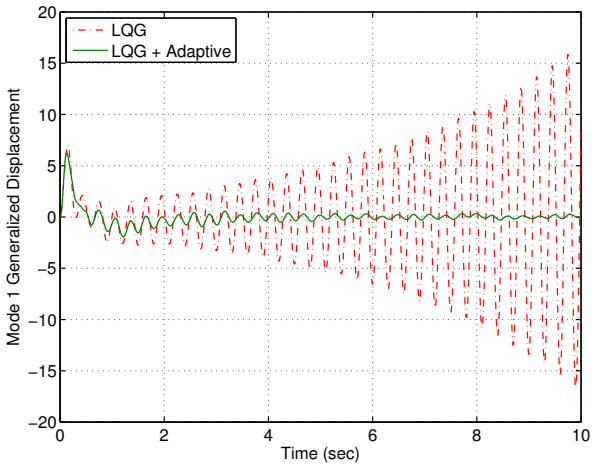

Figure 56: Mode 1 Generalized Displacement Response with and without Adaptive Augmentation Controller

Figure 58 is the plot of the time history of the virtual control command for the output feedback LQG controller with and without the adaptive augmentation controller. The largest amplitude of the stabilizing virtual control command for the adaptive augmentation controller is 6.22°. The linear mapping between the virtual control command and the physical control com-

mands result in 1.56^{o} which meets the physical constraints of 2° on the relative deflection of the VCCTEF.

This study demonstrates the feasibility of active flutter suppression control for increasing the flutter boundary for a flexible wing design with a degraded flutter margin. The use of active flutter suppression does require power which should be accounted for in the overall drag reduction strategy using adaptive aeroelastic wing shaping control technology.

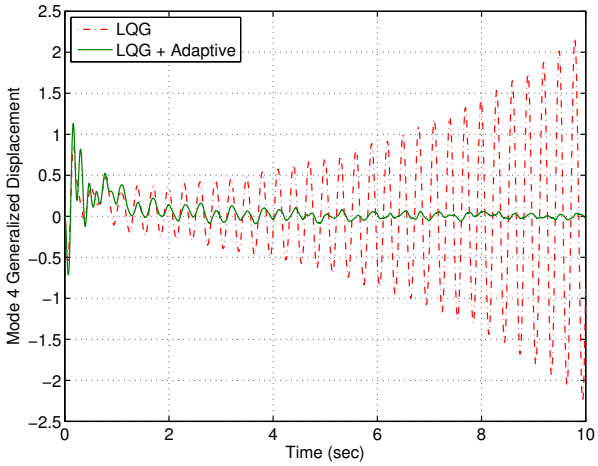

Figure 57: Mode 4 Generalized Displacement Response with and without Adaptive Augmentation Controller

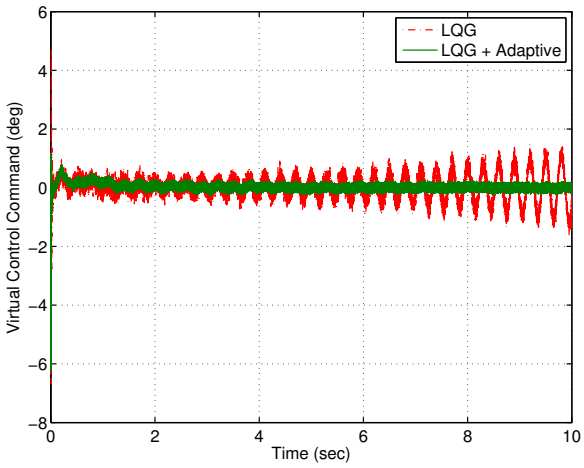

Figure 58: Virtual Control Command with and without Adaptive Augmentation Controller

7 MULTI-OBJECTIVE FLIGHT CONTROL FOR ADAPTIVE WING TECHNOLOGY

Flight control design for conventional aircraft has a long heritage with single-axis control design whereby the elevator is used for pitch control, the aileron (or spoiler) is used for roll control, and the rudder is used for yaw control. The VCCTEF is a multi-functional new type of aerodynamic control surfaces having multiple distributed control surface elements. In the presence of multiple control surfaces such as the VCCTEF, the single-objective flight control tasks such as a pitch command need to be re-examined. A new flight control paradigm should be considered if such control effectors are to become operational someday. In the presence of increased wing flexibility, the conventional rigid-body flight control design may become insufficient since any aircraft maneuvers can potentially excite aeroelastic modes. Currently, in a conventional flight control design, this is addressed passively via ASE notch filtering. Maneuver loads can potentially limit how fast a maneuver can be commanded. Given the availability of multiple control surfaces, a typical flight control design would have to consider additional requirements: 1) minimum drag during transition from one command set point to another, 2) aeroelastic mode suppression, 3) maintaining load alleviation of aeroelastic gust and maneuver load responses within the allowable limits, 4) maintaining acceptable pilot handling qualities based on frequency and damping of the aircraft rigid-body modes, and perhaps other requirements.

To address all of these flight control objectives simultaneously can be a challenging flight control design and would be impossible if there are not sufficient control effectors to accomplish these objectives. A multi-objective flight control and optimization framework can be developed to address the needs for satisfying multiple, competing flight control requirements. A multi-objective flight control framework has been developed to address some of these multi-disciplinary interactions in a flexible wing aircraft employing adaptive aeroelastic wing shaping control technology. A multi-objective flight control system is proposed to simultaneously gain aerodynamic efficiency and maintain traditional pilot command-tracking tasks for guidance and navigation. A multi-objective optimal control design has been developed to address drag minimization during maneuvers in conjunction with aeroelastic mode suppression control.

Multi-objective flight control design is considered to be an enabling technology for adaptive aeroelastic wing shaping control technology. A typical flight control design usually takes into account different sets of re-

quirements for performance and stability that must be considered during a design process. Performance in the context of flight control usually implies the ability for a flight control system to follow a pilot command. However, a new notion of aerodynamic performance is introduced into the flight control framework. The goal of the new vehicle is to achieve low drag through adaptive aeroelastic wing shaping control actuation. Thus, drag penalty due to the VCCTEF should be considered in a flight control design. Hence, a new concept of drag-cognizant multi-objective flight control is proposed to not only achieve a pilot command-following objective but also a drag reduction objective [2, 30] during maneuvers such as a pitch command or roll command.

Stability is of paramount importance for any flight vehicle. Structural flexibility of airframes including wings can cause significant aeroelastic interactions that can degrade vehicle stability margins, potentially leading to loss of control. There exists a trade-off between the desire of having light-weight, flexible structures for weight savings and the need for maintaining sufficient robust stability margins from aeroelastic stability perspectives. For flexible wing aircraft, the flutter speed boundary can occur below FAA flutter clearance. Thus, a flight control system must be able to stabilize aeroelastic modes. The VCCTEF system must be designed to achieve this objective. For obvious reasons, it is not acceptable to operate an unstable transport vehicle that relies on feedback control for closed-loop stability. Thus, in practice, passive aeroelastic tailoring in the design process is used to increase flutter margins. The role of a flight control system would then be relegated to stability augmentation as opposed to a more demanding task of stabilization. This is considered more acceptable in the certification framework as aircraft flight control systems already have many stability augmentation design features built in such as yaw and pitch dampers to provide desired damping characteristics to meet pilot handling quality requirements.

Gust and maneuver load alleviation control is also an important part of the overall flight control strategy for flexible aircraft. As flexibility increases, the vehicle aeroelastic response to wind gust disturbances or during a maneuver can result in structural integrity issues as well as handling and ride quality issues. Gust load alleviation control will reduce the aeroelastic response by reactive feedback control or predictive feedforward control using early detection turbulence sensors. Similarly, maneuver loads can be kept to within the operating load envelope by means of maneuver load alleviation control.

In terms of control actuation, the VCCTEF is designed with dual purposes. The two inner chordwise flap segments are driven by shaped memory alloy (SMA) actuators which are slow actuators suitable only for changing the VCCTEF settings for cruise drag optimization either by scheduling or real-time drag optimization. This is considered a guidance feature. For fast-acting flight control functions, the outermost chordwise flap segment is designed to be a fast acting control surface driven by electro-mechanical actuators (EMA). This flap segment is spanned the entire wing and is assumed to have sufficient bandwidth and control power for roll control and aeroelastic mode suppression control.

The multi-objective flight control framework is envisioned to comprise of the following objectives all acting in a synergistic manner: 1) traditional pilot command-following flight control, 2) drag minimization, 3) aeroelastic mode suppression, and 4) gust and maneuver load alleviation. Each of these objectives can be a major control system design in its own rights. Thus, a multi-objective flight control system can be a complex flight control design that takes into account multiple competing requirements to achieve optimal flight control solutions that have the best compromise for these requirements. Figure 59 illustrates an architecture of a multi-objective flight control system [30].

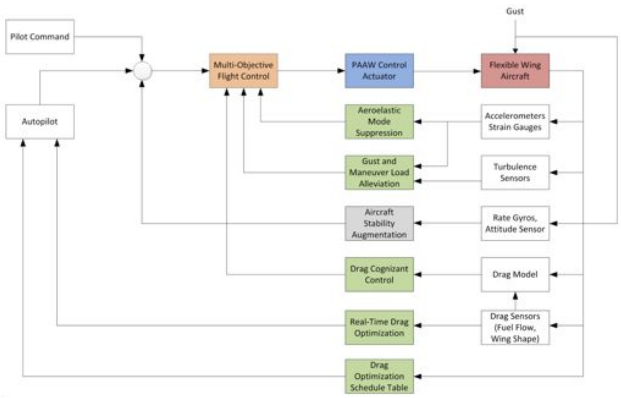

Figure 59: Multi-Objective Flight Control Architecture

In this study, we will consider the first three objectives. We will simplify some aspects of flight control design with a purpose of better illustrating the key salient concepts as opposed to illuminating the detail control theory. Traditional aircraft flight control is well understood, so the focus will be on drag minimization control.

Consider a flight control design for a flight path angle command. Let $x_a = \int_0^t \Delta\gamma d\tau$ be an integral error state of the flight path angle, where the error between the

flight path angle and its command signal is expressed as [30]

$$\Delta\gamma = \theta - \alpha - \gamma_c = A_a x_r - \gamma_c \tag{38}$$

where γ_c is a commanded flight path angle.

Let $x = \begin{bmatrix} x_r & x_e & x_f & x_a \end{bmatrix}^\top$ where $\begin{bmatrix} x_r & x_e & x_f \end{bmatrix}^\top$ is the partitioned state of the reduced-order model, and $u = \begin{bmatrix} u_r & u_v \end{bmatrix}^\top$, then the augmented plant is expressed as

$$\dot{x} = Ax + Bu + z \tag{39}$$

where x_r is the rigid-body state vector, x_e is the aeroelastic state vector including aerodynamic lag states due to unsteady aerodynamics approximation of the Theodorsen's function [31, 32], x_f is the VCCTEF state vector, x_a is the augmented state vector that contains the rigid-body state to be controlled, z is the command vector that contains the command of the rigid-body state to be controlled, u_r is the rigid-body control vectors which include the rudder, aileron, and engine throttle, and u_v is the virtual control vector for the VCCTEF.

An optimal control is designed with the following multi-objective cost function [2, 30]

$$J = \frac{1}{2}\int_0^{t_f} \Big(x_r^\top Q_r x_r + x_e^\top Q_e x_e + x_f^\top Q_f x_f + x_a^\top Q_a x_a + u^\top R u + q_D \Delta C_D \Big) dt \tag{40}$$

where $Q_r > 0$, $Q_e > 0$, $Q_f > 0$, $Q_a > 0$, $R > 0$, and $q_D > 0$.

The first term in the cost function is designed to bound the rigid-body states, the second term to damp out aeroelastic modes, the third term to minimize the VCCTEF states, the fourth term to track the command signal α_c, and the fifth term to minimize the control effort. Hence, the first five terms in the cost function form the standard linear-quadratic regulator (LQR) cost function. The last term is designed to minimize the drag coefficient with q_D as a weighting constant. The coefficient ΔC_D represents the increase in drag relative to the drag in trim condition.

It is assumed that the drag coefficient can be estimated accurately via a drag polar model for which the drag polar parameters are known. Alternatively, a drag model could be estimated in-flight using system identification techniques. The model is derived using aerodynamic strip theory. The wing, fuselage, and horizontal tail surface are divided into strips for which the local drag derivatives are calculated. The total drag polar model can be expressed as

$$C_D = C_{D_0} + C_{L_0}^\top K C_{L_0} + C_{D_x} x + x^\top C_{D_{x^2}} x \tag{41}$$

$$C_{D_x} = 2C_{L_0}^\top K \left(C_{L_x} + C_{L_{\dot{x}}} A \right) \tag{42}$$

$$C_{D_{x^2}} = \left(C_{L_x} + C_{L_{\dot{x}}} A \right)^\top K \left(C_{L_x} + C_{L_{\dot{x}}} A \right) \tag{43}$$

where K is a diagonal matrix containing the drag polar parameter of each strip, C_{D_0} is a scalar value representing the zero-lift drag coefficient, C_{L_0} is a column vector containing the trim state lift coefficient of each strip, and C_{L_x} and $C_{L_{\dot{x}}}$ are matrices containing the lift stability and control derivatives for each strip. Note that the control input u does not contribute directly to the drag, since it is composed entirely of control commands.

The drag-cognizant multi-objective optimal control is then given by

$$u = K_x x + K_z z + \Lambda_0 \tag{44}$$

$$K_x = -R^{-1} B^\top P \tag{45}$$

$$K_z = -R^{-1} B^\top S \tag{46}$$

$$\Lambda_0 = -R^{-1} B^\top \lambda_0 \tag{47}$$

where P which is the solution to the Ricatti equation, S, and λ_0 are given by

$$PA + A^\top P - PBR^{-1}B^\top P + Q + q_D C_{D_{x^2}} = 0 \tag{48}$$

$$S = \left(PBR^{-1}B^\top - A^\top \right)^{-1} P \tag{49}$$

$$\lambda_0 = \left(PBR^{-1}B^\top - A^\top \right)^{-1} \left(\frac{1}{2} q_D C_{D_x}^\top \right) \tag{50}$$

Especially noteworthy is the term Λ_0, which unlike the two other terms is non-zero even if $x = 0$ and $z = 0$. The term Λ_0 exists due to the linear drag term $q_D C_{D_x} x$ in the cost function and enables the flight controller to trim the aircraft to the minimum drag trim condition using the elevator and VCCTEF.

In the implementation, a state observer is constructed using the Kalman filter optimal estimation method. The Kalman filter receives measurements from available accelerometers. Before the accelerometer measurements can be used in the Kalman filter they need to pass through a low-pass filter. There are two reasons why this is necessary. Firstly, measurement noise is to be filtered out. Secondly, contributions of high frequency modes that are not maintained in the reduced-order model may negatively affect the state estimation. While these high frequency modes do not reach large deflections, they do contribute significantly to the accelerometer output, which leads to a mismatch between the measured output and the predicted output of the reduced-order model that is used to design the Kalman filter. Hence, the cut-off frequency of the low-pass filter should be chosen with the maximum frequency of the elastic modes in the

reduced-order model in mind. In order to minimize the delay of the measurement signal by limiting the phase lag of the low-pass filter, a Bessel filter is used.

Multi-objective flight control can potentially enable a more functional flight control system to take advantages of multiple control surfaces available like the VCCTEF. The benefits of these flaps are driven by the aerodynamic performance objective such as drag minimization. By including a drag minimization objective in the control design, this directly addresses the ultimate goal of the adaptive aeroelastic wing shaping control technology. While this study addresses the inner-loop fast-acting control using the outermost flap segments of the VCCTEF, a more important aspect of multi-objective flight control requirement to truly achieve adaptive aeroelastic wing shaping control technology deals with the outer-loop guidance law for drag minimization during cruise. The two inner flap segments which are driven by lightweight slow-acting SMA actuators are designed to provide adaptive wing shapes during cruise that minimizes drag. This outer-loop guidance can be based on a pre-programmed schedule of flap settings based on aircraft gross weight and flight conditions. Off-line optimization can be used to define these flap settings.

A more potentially game-changing approach to achieving a true adaptive wing is to have the ability to determine the flap settings in real-time based on the current aircraft information. This real-time drag minimization control strategy can increase the potential benefits of adaptive aeroelastic wing shaping control technology like the VCCTEF. However, drag minimization control can be challenging in many aspects. First of all, drag sensors must be available for real-time drag minimization control. A previous study conducted by NASA Armstrong Flight Research Center has developed a peak-seeking optimization for minimizing the fuel flow as an indication of drag [33]. Test flight on NASA F/A-18 research aircraft, tail number 853, indicates fuel flow reduction is achieved with this method. Since drag penalty is directly related to the wing shape which changes continuously in-flight at off-design flight control, it may be possible to infer drag from a wing shape sensor such as the fiber optic shape sensor (FOSS) being developed at NASA Armstrong Flight Research Center. Other types of sensors for drag measurements could be developed in the future.

A real-time drag minimization control has been proposed in a recent study [30]. Consider a steady-state cruise flight during which the dynamics of aircraft, flexible wing, and flaps are no longer considered important, so that the quasi-steady state drag coefficient can be expressed as

$$C_D = C_{D_0} + \left(C_{L_0} + C_{L_x} x + C_{L_u} u\right)^\top K \times \\ \times \left(C_{L_0} + C_{L_x} x + C_{L_u} u\right) \quad (51)$$

It should be noted that u is no longer a command vector, but is a control vector such as elevator deflection δ_e, thrust δ_T, and all the VCCTEF flaps. It is also noted that the drag polar parameter K is usually not known precisely. For that matter, the lift derivatives are also not known precisely. Thus, one aspect of real-time drag minimization is parameter estimation. Let $\hat{C}_D$ be the estimate of C_D which is assumed to be measurable by suitable sensors. The drag coefficient can be re-written as

$$\hat{C}_D = \Theta^\top \Phi\left(x, u\right) \quad (52)$$

where $\Theta = \begin{bmatrix} C_{D_0} + C_{L_0}^\top K C_{L_0} & C_{L_0} K C_{L_x} & C_{L_0} K C_{L_u} & C_{D_{x^2}} & C_{D_{xu}} & C_{D_{u^2}} \end{bmatrix}^\top$, $\Phi\left(x, u\right) = \begin{bmatrix} 1 & x^\top & u^\top & ele\left(xx^\top\right) & ele\left(xu^\top\right) & ele\left(uu^\top\right) \end{bmatrix}^\top$, and $ele\left(A\right)$ is the element-wise column vector of A.

The drag parameter estimation can be computed in real time using the following least-squares method

$$\dot{\Theta} = -\Gamma \nabla J_\Theta\left(\Theta\right) = -\Gamma \Phi\left(x, u\right)\left[\Phi^\top\left(x, u\right)\Theta - C_D\right] \quad (53)$$

where Γ is a tuning parameter.

As an aircraft passes through many different flight states in-flight, information on drag, aircraft states, and control can be collected in flight computers for post-processing. These past data can be used to estimate drag in a least-squares sense. As more data become available, and assuming that the drag measurements are sufficiently reliable and accurate, then the least squares estimation should yield a good approximation of the drag model. Using this drag model, the control flaps can be computed for real-time drag minimization using a real-time drag minimization control algorithm as

$$u = -\frac{1}{2}\hat{C}_{D_{u^2}}^{-1}\left(\hat{C}_{D_u} + \hat{C}_{D_{xu}}^\top x\right) \quad (54)$$

However the problem with this approach could lie in the matrix inversion of $\hat{C}_{D_{u^2}}$. This matrix could be small. So when it is inverted, a large control solution may result. So, an adaptive algorithm could be used instead

$$\dot{u} = -\Gamma\left(\hat{C}_{D_u} + \hat{C}_{D_{xu}}^\top x + 2\hat{C}_{D_{u^2}} u\right) \quad (55)$$

It should be noted that the full state information may not be available such as the aeroelastic states. Therefore, suffice to say a Kalman filter will have to be designed for state estimation in conjunction with real-time drag minimization control.

Numerical simulations were performed to assess the performance of the multi-objective flight control. The simulations were run using a coupled nonlinear 6-DOF flight dynamic and full-order ASE model. The full-order model includes in total 198 symmetric and anti-symmetric elastic modes. The unsteady aerodynamics of the elastic wing and the VCCTEF are approximated using a second-order approximation of the Theodorsen's function. The total number of states in this model is 1463. All simulations were initialized in trimmed cruise condition at 36,000 ft altitude and Mach 0.797. The initial trim was achieved using the elevator and zero VCCTEF deflection.

The following three controllers are evaluated [30]:

- C_1 is a baseline single-objective LQR controller for tracking of a flight path angle command. Since state feedback is available for the rigid-body and VCCTEF states, controller C_1 does not require the use of a Kalman filter.
- C_2 is a double-objective LQG controller for tracking of a flight path angle command and aeroelastic mode suppression. The control model has 10 elastic states and uses a first-order approximation of the Theodorsen's function for modeling unsteady aerodynamics. This leads to a Kalman filter with 40 state variables; 20 generalized modal coordinates and 20 aerodynamic lag states.
- C_3 is a triple-objective LQG controller for tracking of a flight path angle command, aeroelastic mode suppression, and drag minimization. It is based on the same linear reduced-order ASE state-space model of the ESAC and VCCTEF as used for controller C_2 and has the same Kalman filter state.

The controllers are given a flight path angle command input, as shown in Figure 60. After the controller is engaged at $t = 0$ sec, the aircraft performs a climb at $\gamma = 1°$ (approximately 110 ft per nautical mile) and subsequently levels off. The altitude change in response to the flight path angle command is shown in Figure 61.

The corresponding pitch rate responses are shown in Figure 62. In particular, the response corresponding to controller C_1 has large transients. This illustrates the influence of aeroelastic modes on the rigid-body flight dynamics. The responses of controllers C_2 and C_3 are similar.

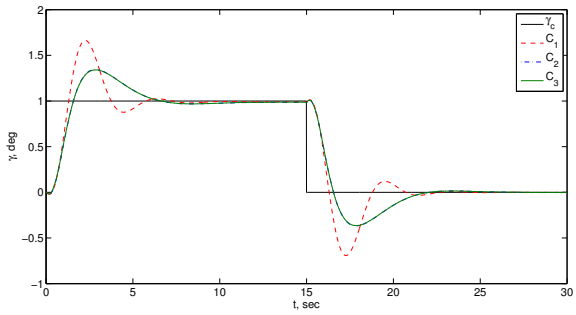

Figure 60: Flight Path Angle Command and Responses

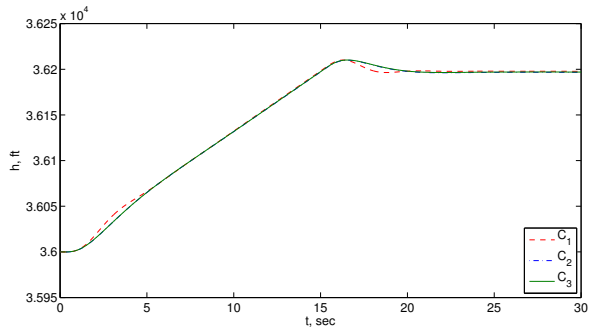

Figure 61: Altitude Responses

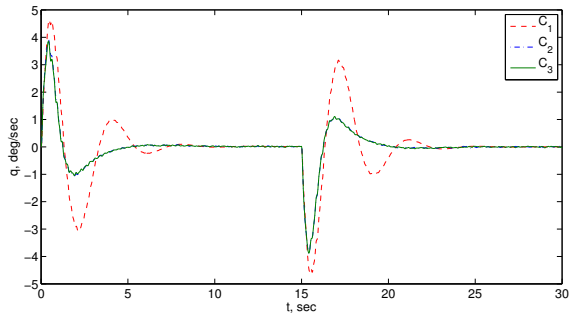

Figure 62: Pitch Rate Responses

The modal responses of the first three symmetric modes are shown in Figures 63 to 65. It can indeed be seen that the modal excitation is larger for controller C_1. Controllers C_2 and C_3 are more capable of damping out the aeroelastic modes. The first symmetric mode is the first bending mode and positive excitation corresponds to upward tip deflection. It should be noted that due to the static aeroelastic

deformation of the wing in trim condition, the total vertical tip deflection is upward throughout the simulation for all controllers. The responses corresponding to controllers C_2 and C_3 are similar for the first two modes. The third symmetric mode is the first torsion mode. The response corresponding to controller C_3 shows a negative response, which corresponds to nose-down twist of the wing in steady-state climb and level flight. In essence, controller C_3 re-trims the aircraft to minimize drag since it is a drag-cognizant multi-objective flight controller.

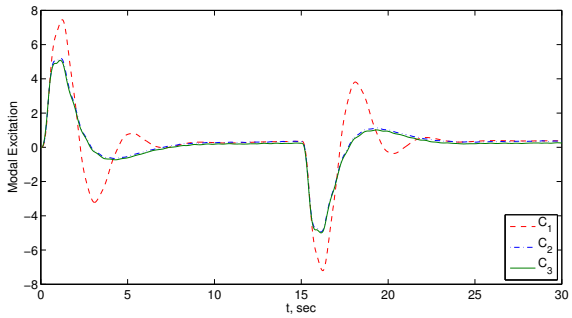

Figure 63: First Symmetric Modal Responses

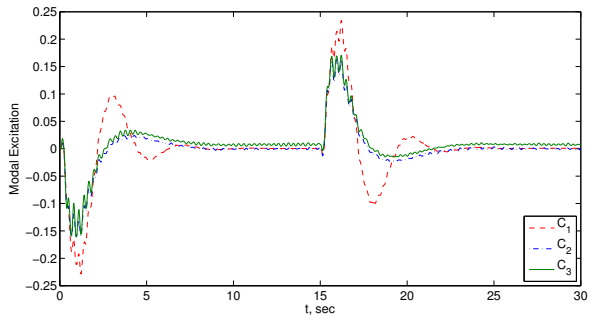

Figure 64: Second Symmetric Modal Responses

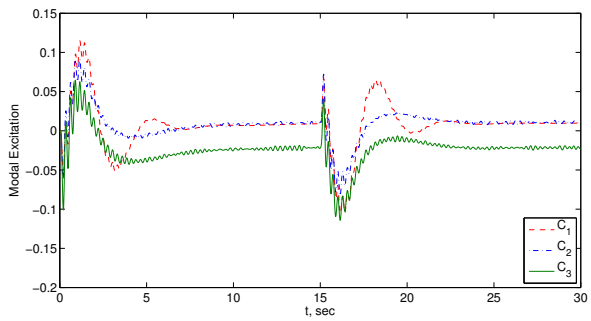

Figure 65: Third Symmetric Modal Responses

Figure 66 shows the incremental drag coefficient relative to the drag coefficient in the trim state. Controller C_1 results in a larger incremental drag coefficient in transient than for the two other controllers. The incremental drag coefficients in trim are similar for controllers C_1 and C_2. It can be observed that the drag coefficient corresponding to the drag-cognizant multi-objective flight controller C_3 is lower than the those corresponding controllers C_1 and C_2 without drag minimization.

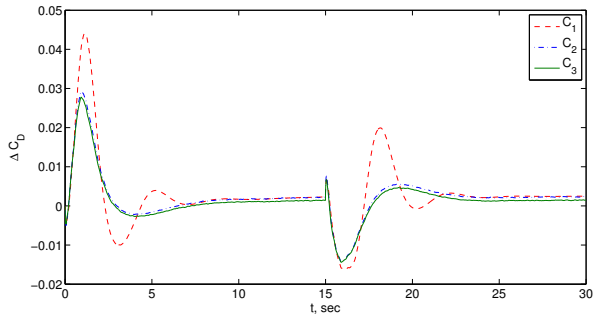

Figure 66: Drag Coefficient Responses

The lift-to-drag ratio curves can be seen in Figure 67. The values in the figure are normalized to the initial trim lift-to-drag ratio obtained by trimming the aircraft using the elevator without the VCCTEF deflection. During steady-state climb and level flight, controller C_3 achieves an increase in lift-to-drag ratio of approximately 4% relative to controllers C_1 and C_2.

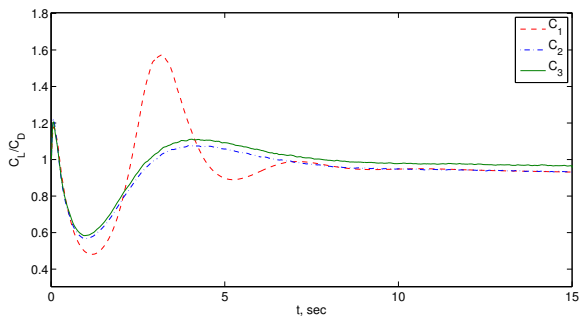

Figure 67: Lift-to-Drag Ratio Responses

This study demonstrates the potential benefits of multi-objective flight control as an enabling technology for adaptive aeroelastic wing shaping control. The inclusion of drag minimization in aircraft flight control systems can further extend the capability of adaptive aeroelastic wing shaping control technology to achieve increased fuel efficiency of future transport aircraft.

8 CONCLUSION

This paper summarizes the development of a variable camber continuous trailing edge flap system for use in adaptive aeroelastic wing shaping control. The VCCTEF is a multi-functional flap system capable of shaping wing aeroelastic deflections to achieve optimal spanwise lift distribution for drag reduction, as well as suppressing flutter modes, and enabling high-lift and roll control. Aerodynamic simulations and wind tunnel tests show that drag reduction achieved by the VCCTEF could be significant. To truly realize adaptive wing technology, multi-objective flight control is an enabling technology that is capable of achieving multiple flight control objectives simultaneously. These objectives include pilot command-following, ASE mode suppression, load alleviation, and drag minimization. Simulations demonstrate the potential benefits of multi-objective flight control for drag minimization. Future transport aircraft could potentially be more fuel efficient by incorporating adaptive aeroelastic wing shaping control technology in the aircraft design.

References

[1] Nguyen, N., "Elastically Shaped Future Air Vehicle Concept," NASA Innovation Fund Award 2010 Report, October 2010, Submitted to NASA Innovative Partnerships Program, http://ntrs.nasa.gov/archive/nasa /casi.ntrs.nasa.gov/20110023698.pdf

[2] Nguyen, N. and Urnes, J., "Aeroelastic Modeling of Elastically Shaped Aircraft Concept via Wing Shaping Control for Drag Reduction," AIAA Atmospheric Flight Mechanics Conference, AIAA-2012-4642, August 2012.

[3] Nguyen, N., Trinh, K., Reynolds, K., Kless, J., Aftosmis, M., Urnes, J., and Ippolito, C., "Elastically Shaped Wing Optimization and Aircraft Concept for Improved Cruise Efficiency," 51st AIAA Aerospace Sciences Meeting, AIAA-2013-0141, January 2013.

[4] Boeing Report No. 2012X0015, "Development of Variable Camber Continuous Trailing Edge Flap System," Submitted to NASA, October 4, 2012.

[5] Boeing Report No. 2014X0030, "Development of Variable Camber Continuous Trailing Edge Flap System for B757 Configured with a More Flexible Wing," Submitted to NASA, September 27, 2014.

[6] Urnes, J., Nguyen, N., Ippolito, C., Totah, J., Trinh, K., and Ting, E., "A Mission Adaptive Variable Camber Flap Control System to Optimize High Lift and Cruise Lift to Drag Ratios of Future N+3 Transport Aircraft," 51st AIAA Aerospace Sciences Meeting, AIAA-2013-0214, January 2013.

[7] Urnes, J., Morris, C., Sheahan, J., Dykman, J., and Klingman, D., "Control System Design for a Variable Camber Continuous Trailing Edge Flap System on an Elastic Wing," 55th AIAA/ASME/ASCE/AHS/ASC Structures, Structural Dynamics, and Materials Conference, AIAA-2014-0835, January 2014.

[8] Dykman, J., Truong, H., and Urnes, J., "Active Control for Elastic Wing Structure Dynamic Modes," 56th AIAA/ASCE/AHS/ASC Structures, Structural Dynamics, and Materials Conference, AIAA-2015-1842, January 2015.

[9] Precup, N., Mor, M., and Livne, E., "Design, Construction, and Tests of an Aeroelastic Wind Tunnel Model of a Variable Camber Continuous Trailing Edge Flap (VCCTEF) Concept Wing," 32nd AIAA Applied Aerodynamics Conference, AIAA-2014-2442, June 2014.

[10] Nguyen, N., Precup, N., Urnes, J., Nelson, C., Lebofsky, S., Ting, E., and Livne, E., "Experimental Investigation of a Flexible Wing with a Variable Camber Continuous Trailing Edge Flap Design," 32nd AIAA Applied Aerodynamics, AIAA 2014-2441, June 2014.

[11] Precup, N., Mor, M., and Livne, E., "The Design, Construction, and Tests of a Concept Aeroelastic Wind Tunnel Model of a High-Lift Variable Camber Continuous Trailing Edge Flap (HL-VCCTEF) Wing Configuration," 56th AIAA/ASCE/AHS/ASC Structures, Structural Dynamics, and Materials Conference, AIAA-2015-1406, January 2015.

[12] Nguyen, N., Precup, N., Livne, E., Urnes, J., Dickey, E., Nelson, C., Chiew, J., Rodriguez, D., Ting, E., and Lebofsky, S., "Wind Tunnel Investigation of a Flexible Wing High-Lift Configuration with a Variable Camber Continuous Trailing Edge Flap Design," 33rd AIAA Applied Aerodynamics Conference, AIAA-2015-2417, June 2015.

[13] Kaul, U. and Nguyen, N., "Drag Optimization Study of Variable Camber Continuous Trailing Edge Flap (VCCTEF) Using OVERFLOW," 32nd AIAA Applied Aerodynamics, AIAA 2014-2444, June 2014.

[14] Lebofsky, S., Ting, E., and Nguyen, N., "Aeroelastic Modeling and Drag Optimization of Flexible Wing Aircraft with Variable Camber Continuous Trailing Edge Flap," 32nd AIAA Applied Aerodynamics, AIAA 2014-2443, June 2014.

[15] Lebofsky, S., Ting, E., and Nguyen, N., "Multidisciplinary Drag Optimization of Reduced Stiffness Flexible Wing Aircraft With Variable Camber Continuous Trailing Edge Flap," 56th AIAA/ASME/ASCE/AHS/ASC Structures, Structural Dynamics, and Materials Conference, AIAA-2015-1408, January 2015.

[16] Rodriguez, D., Aftosmis, M., Nemec, M., and Anderson, G., "Optimized Off-Design Performance of Flexible Wings with Continuous Trailing-Edge Flaps," 56th AIAA/ASCE/AHS/ASC Structures, Structural Dynamics, and Materials Conference, AIAA-2015-1409, January 2015.

[17] Ting, E., Nguyen, N., and Trinh, K., "Static Aeroelastic and Longitudinal Trim Model of Flexible Wing Aircraft Using Finite-Element Vortex-Lattice Coupled Solution," 55th AIAA/ASME/ASCE/AHS/ASC Structures, Structural Dynamics, and Materials Conference, AIAA-2014-0837, January 2014.

[18] Stahara, S., " Operational Manual for Two-Dimensional Transonic Code TSFOIL," NASA Contractor Report 3064, December 1978.

[19] Nguyen, N., Ting, E., Nguyen, D., Dao, T., and Trinh, K., "Coupled Vortex-Lattice Flight Dynamic Model with Aeroelastic Finite-Element Model of Flexible Wing Transport Aircraft with Variable Camber Continuous Trailing Edge Flap for Drag Reduction," AIAA Atmospheric Flight Mechanics, AIAA-2013-4746, August 2013.

[20] Rodriguez, D., Aftosmis, M., Nemec, M., and Smith, S., "Static Aeroelastic Analysis with an Inviscid Cartesian Method," 55th AIAA/ASME/ASCE/AHS/ASC Structures, Structural Dynamics, and Materials Conference, AIAA-2014-0836, January 2014.

[21] Liu, Y., Bai, J., and Livne, E., "Robust Optimization of Variable Camber Continuous Trailing Edge Flap System Action Using Stochastic Kriging," 33nd AIAA Applied Aerodynamics Confererence, AIAA-2015-2421, June 2015.

[22] Chen, P., Zhou, Z., Ghoman, S., and Falkiewicz, N., "Low-Weight Low-Drag Truss-Braced Wing Design Using Variable Camber Continuous Trailing Edge Flaps," 56th AIAA/ASME/ASCE/AHS/ASC Structures, Structural Dynamics, and Materials Conference, AIAA-2015-1176, January 2015.

[23] Lebofsky, S., Ting, E., Trinh, K., and Nguyen, N., "Optimization for Load Alleviation of Truss-Braced Wing Aircraft With Variable Camber Continuous Trailing Edge Flap," 33nd AIAA Applied Aerodynamics Confererence, AIAA-2015-2723, June 2015.

[24] Nguyen, N., Swei, S., and Ting, E., "Adaptive Linear Quadratic Gaussian Optimal Control Modification for Flutter Suppression of Adaptive Wing," AIAA Infotech@Aerospace Conference, AIAA 2015-0118, January 2015.

[25] Nguyen, N., Ting, E., and Lebofsky, S., "Aeroelastic Analysis of Wind Tunnel Test Data of a Flexible Wing with a Variable Camber Continuous Trailing Edge Flap," 56th AIAA/ASME/ASCE/AHS/ASC Structures, Structural Dynamics, and Materials Conference, AIAA-2015-1405, January 2015.

[26] Yamauchi, G. K. and John, W., "Trends of Reynolds Number Effects on TWQ - Dimensional Airfoil Characteristics for Helicopter Rotor Analyses," NASA TM 84363, April 1983.

[27] Stanford University AA241 Course Website, "Maximum Lift Prediction - Specific Conceptual Design Methods," http://adg.stanford.edu/aa241/highlift/clmaxest.html.

[28] White, F. M., *Viscous Fluid Flow*, McGraw-Hill, Second Edition, 1991.

[29] Nguyen, N., Ting, E., Nguyen, D., and Trinh, K., "Flutter Analysis of Mission-Adaptive Wing with Variable Camber Continuous Trailing Edge Flap," 55th AIAA/ASME/ASCE/AHS/ASC Structures, Structural Dynamics, and Materials Conference, AIAA-2014-0839, January 2014.

[30] Nguyen, N. and Tal, E., "A Multi-Objective Flight Control Approach for Performance Adaptive Aeroelastic Wing," 56th AIAA/ASME/ASCE/AHS/SC Structures, Structural Dynamics, and Materials Conference, AIAA-2015-1843, January 2015.

[31] Nguyen, N., Ting, E., Nguyen, D., and Trinh, K., "Flight Dynamic Modeling and Stability Analysis of Flexible Wing Generic Transport Aircraft," 55th AIAA/ASME/ASCE/AHS/ASC Structures, Structural Dynamics, and Materials Conference, AIAA-2014-1040, January 2014.

[32] Tal, E., Nguyen, N. and Ting, E., "Comparison of Unsteady Aerodynamics Approximations for Time-Domain Representation of Frequency-Independent Aeroelastic State-Space Models," 56th AIAA/ASME/ASCE/AHS/ASC Structures, Structural Dynamics, and Materials Conference, AIAA-2015-1841, January 2015.

[33] Brown, N. and Schaefer, J., "Peak-Seeking Optimization of Trim for Reduced Fuel Consumption: Flight-Test Results," AIAA Guidance, Navigation, and Control Conference, AIAA-2013-5171, August 2013.